nature communications

Article

https://doi.org/10.1038/s41467-024-50769-0

Catalytic activity of violet phosphorus-based nanosystems and the role of metabolites in tumor therapy

Received: 13 November 2023

Accepted: 22 July 2024

Published online: 08 August 2024

Check for updates

Hanjie Zhang[1], Yitong Zhang[1], Yushi Zhang[1], Hanyue Li[1], Meitong Ou[1], Yongkang Yu[2], Fan Zhang[1], Huijuan Yin[1,3], Zhuo Mao[1] ✉ & Lin Mei[1] ✉

Although nanocatalytic medicine has demonstrated its advantages in tumor therapy, the outcomes heavily relie on substrate concentration and the metabolic pathways are still indistinct. We discover that violet phosphorus quantum dots (VPQDs) can catalyze the production of reactive oxygen species (ROS) without requiring external stimuli and the catalytic substrates are confirmed to be oxygen (O_2) and hydrogen peroxide (H_2O_2) through the computational simulation and experiments. Considering the short of O_2 and H_2O_2 at the tumor site, we utilize calcium peroxide (CaO_2) to supply catalytic substrates for VPQDs and construct nanoparticles together with them, named VPCaNPs. VPCaNPs can induce oxidative stress in tumor cells, particularly characterized by a significant increase in hydroxyl radicals and superoxide radicals, which cause substantial damage to the structure and function of cells, ultimately leading to cell apoptosis. Intriguingly, O_2 provided by CaO_2 can degrade VPQDs slowly, and the degradation product, phosphate, as well as CaO_2-generated calcium ions, can promote tumor calcification. Antitumor immune activation and less metastasis are also observed in VPCaNPs administrated animals. In conclusion, our study unveils the anti-tumor activity of VPQDs as catalysts for generating cytotoxic ROS and the degradation products can promote tumor calcification, providing a promising strategy for treating tumors.

Nanocatalytic medicine, a subdiscipline of tumor nanomedicine, is achieved by introducing nano-sized catalysts to consume or produce substances for tumor elimination[1–4]. Typically, reactive oxygen species (ROS) can be catalytically generated and attack macromolecules of cells, thus destroying cell structure and function and inducing tumor apoptosis[5–7]. Here are two ways of catalytically generating ROS: externally- and in situ environmentally- stimulated catalytic reactions. When a catalyst is introduced, the reaction can be activated by external physical stimuli like light, ultrasound, or electricity to generate ROS[8–10]. Otherwise, characteristics of the local microenvironment (e.g., acidity) can stimulate catalytic reactions, such as Fenton reactions[11–13].

However, clinical translation of catalytic therapy based on ROS generation still faces the following problems: First, reaction substrate is insufficient in tumor site. ROS is typically generated from small molecules containing oxygen element, such as O_2 and H_2O_2, which cannot be sufficiently provided by deoxygenated[14,15], low-H_2O_2 content

[1]State Key Laboratory of Advanced Medical Materials and Devices, Tianjin Key Laboratory of Biomedical Materials, Key Laboratory of Biomaterials and Nanotechnology for Cancer Immunotherapy, Institute of Biomedical Engineering, Chinese Academy of Medical Sciences and Peking Union Medical College, Tianjin, PR China. [2]School of Chemistry, Chemical Engineering and Biotechnology, Nanyang Technological University, Singapore, Singapore. [3]Integrative regeneration laboratory, Institute of Biomedical Engineering, Chinese Academy of Medical Sciences and Peking Union Medical College, Tianjin, PR China. ✉e-mail: maozhuo313@tju.edu.cn; meilin@bme.pumc.edu.cn

(50–100 μM)[16] tumor microenvironment. Second, catalytic reactions have strict requirements on environmental characteristics, such as pH value. Taking classical Fenton reaction, the generation of ·OH is accompanied by the oxidation of Fe^{2+} to Fe^{3+}, while the reaction could be ceased due to the precipitating Fe^{3+} to hydrous oxyhydroxide when the pH is higher than 3.5[17–19]. Before everything, any degradation products and metabolites may be a potential cause of side effects or new opportunities for treatment[20,21], and the metabolism of catalysts and subsequent biological effects is always unstated. Therefore, multidirectional regulation of the composition, structure, and properties of nanocatalysts to maximize their catalytic efficiency in tumor microenvironment and thorough understanding of the metabolic pathways are two keys to improve the clinical application potential of nanocatalytic therapy.

Here, we propose the most stable phosphorus single crystal, violet phosphorus (Hittorf's violet phosphorus, VP)[22], as a catalyst for the application of tumor catalytic medicine. Firstly, we synthesized violet phosphorus quantum dots (VPQDs) and predicted the band structures of VP and catalytic mechanism based on first-principles calculations based on density functional theory (DFT), which is in accordance with experimental results that two species of oxygen radicals can be generated in acidic condition. Next, nanoparticles consisting of VPQDs, calcium peroxide, sodium hyaluronate (HA), and polyacrylic acid (PAA) were synthesized by a one-pot method, named VPCaNPs, for self-catalyzing ROS generation. The metabolites of VPQDs and CaO_2, phosphate ions and calcium ions, respectively, can ultimately trigger cell calcification (Fig. 1). Additionally, VPCaNPs can also induce the antitumor immune response in mice. In short, the full use of the inherent catalytic function of VPQDs, the biological effect of degradation product of VPCaNPs, and the immune activation ability of VPCaNPs can effectively inhibit tumor growth and lung metastasis as well as reducing systematic toxicity.

Results

Fabrication and verification of VPQDs

The scheme of VPQDs synthesis is illustrated in Fig. 2a, which underwent a successive process of liquid exfoliation and solvothermal reaction. In detail, layered VP powder was ground in NMP solution and the VP/NMP suspension was then subjected to ultrasonic-assisted liquid exfoliation for at least 12 h on ice bath. After centrifugation and removing large precipitation, the supernatant (VP nanosheets, VPNSs) was transferred into polytetrafluoroethylene reactors for solvothermal reaction. VPQDs were obtained after concentrated by distill and dialysis in water. VP crystals are layered and a single layer composes two perpendicular rows of phosphorus tubes linked by chemical bonds (Fig. 2b). The layers are held together by van der Waals forces, which are weak and can be easily destroyed by sonication. The high-temperature and high-pressure environment of the solvent thermal reaction are beneficial to further attack and break of the covalent P–P bonds by NMP molecules. The obtained VPQDs have a size of around 2.25 nm according to transmission electron microscope image (Fig. 2c) and a thickness of 1–3 nm according to atomic force microscope (AFM) image (Fig. 2d), 2–3 times of the thickness of the calculated VP monolayer (9.64 Å, Fig. 2b). As shown in Fig. 2e and Supplementary Fig. 1, the VPQDs can fluoresce when stimulated by blue to ultraviolet light, which is consistent with previous reports[23,24].

To confirm the as-prepared quantum dots are VP, we conducted high-resolution transmission electron microscopy (HRTEM). The representative image in Fig. 2f clearly showed a crystalline structure. The corresponding fast Fourier transform (FFT) image in Fig. 2g showed typical diffraction spots and rings. The measured radii were used to calculate the interplanar spacing (d) according to Bragg's law, and the Miller indices (hkl) of each diffraction spot or ring can be calibrated by comparison with the d value in the standard powder diffraction file of VP (PDF#44-0906). The most conspicuous diffraction spots (on blue dotted circle) were indexed to the (400) planes and the corresponding inverse FFT image showed the lattice fringes was around 2.19 Å. The yellow and red marked diffraction rings were related to (212) and (013) planes, respectively. Another HRTEM image (Supplementary Fig. 2) exhibited obvious lattice fringes with spaces of 2.23 Å, which can be also indexed to the (400) planes, confirming VP crystal was not completely broken during high-energy mechanical forces and solvent attack. Also, X-ray diffraction (XRD) spectrum (Fig. 2h and Supplementary Fig. 3) inferred successful synthesis of VPQDs. The simulated XRD spectral of bulk VP (red line), available via Cambridge Crystallographic Data Centre (ICSD 131503), is supposed to exhibit crystal planes that can be detected. In experiments, peak positions will remain the same as simulated pattern, but relative intensities of the peaks can change due to instrumental effects and relative position between X-ray and most crystalline grains[25]. Each peak position of VPNSs (blue line in supplementary Fig. 3) could be found in the spectrum of simulated bulk VP and the whole spectrum was consistent well with the standard card of VP (PDF#44-0906). Also, the strong 2θ diffraction peaks at 16.2°, 24.5° and 32.9° were consistent with reported data[23]. As is described in the Scherrer equation, decrease in crystallite size can cause diffraction-peak broadening increase[26]. Therefore, the size range (below 5 nm) of as-prepared VPQDs presents difficulty for analysis due to broadened peaks (such as a broad peak around 21°) and low signal-to-noise ratios. Nevertheless, we still found that small peaks at 14.8° and 26.4° in the spectrum (blue line in Fig. 2h) can be attributed to (013) and (212) planes, respectively, which were well matched with FFT results of HRTEM image (Fig. 2g). Raman plot could be another evidence to confirm crystal form. As shown in supplementary Fig. 4, VPNSs shared almost the same Raman spectrum with bulk VP. Despite the low sensitivity of measuring Raman shift of quantum dots, a typical region (dashed box)[27] indicated that the as-prepared quantum dots were still VP. In conclusion, the above results evidently certify the successful preparation of VPQDs.

VP-catalyzed ROS production and the mechanism

The catalytic capacity of VPQDs in different substrate environment and pH was investigated through the general ROS probe, 1,3-Diphenylisobenzofuran (DPBF). As shown in Fig. 3a, DPBF could be consumed mediated by VPQDs in an O_2-sufficient environment and this phenomenon is more obvious under an acidic environment (pH = 6.5). Similarly, in the H_2O_2-sufficient solution, DPBF obviously degraded by VPQDs under the acidic environment (Fig. 3b). These results indicate that acidic environment is conducive to catalytic reaction, suggesting that the catalytic effect of VPQDs in acidic tumor microenvironment may be higher than that in normal physiological conditions. To confirm the species of produced ROS, electron spin resonance (ESR) experiments were conducted. The results show that VPQDs could mediate $\cdot O_2^-$ production in an oxygenated environment (Fig. 3c) and ·OH could be generated in H_2O_2-sufficient condition (Fig. 3d). In addition, ESR test confirmed that VP could catalyzed the decomposition of H_2O_2 but not H_2O into ·OH (Supplementary Fig. 5) without external stimuli, indicating that the catalytic reactivity and efficiency of Fenton-like pathway mediated H_2O_2 homolytic cleavage is higher than H_2O heterolytic cleavage pathway.

The relative positions among energy edges of catalyst and reduction-oxidation potentials reflect the probability of redox reactions. To estimate experimental band gap (E_g) of VPQDs, UV-vis diffuse reflection test was conducted and the diffuse reflectance spectrum (DRS) was shown in Fig. 3e. The corresponding Tauc plot of DRS plot (insert Fig. 3e) according to Kubelka-Munk formula revealed the direct E_g of lyophilized VPQDs was approximately 1.64 eV. The valence band maximum (E_{VB}) was measured to be around 0.53 eV via a narrow scan from −5 to 30 eV through X-ray photoelectron spectroscopy (XPS) (Fig. 3f). And the estimated conduction band minimum (E_{CB}) was −1.11 eV by subtracting E_g from E_{VB}. For facilitate comparison of the redox potential and the band edges, the normal hydrogen electrode

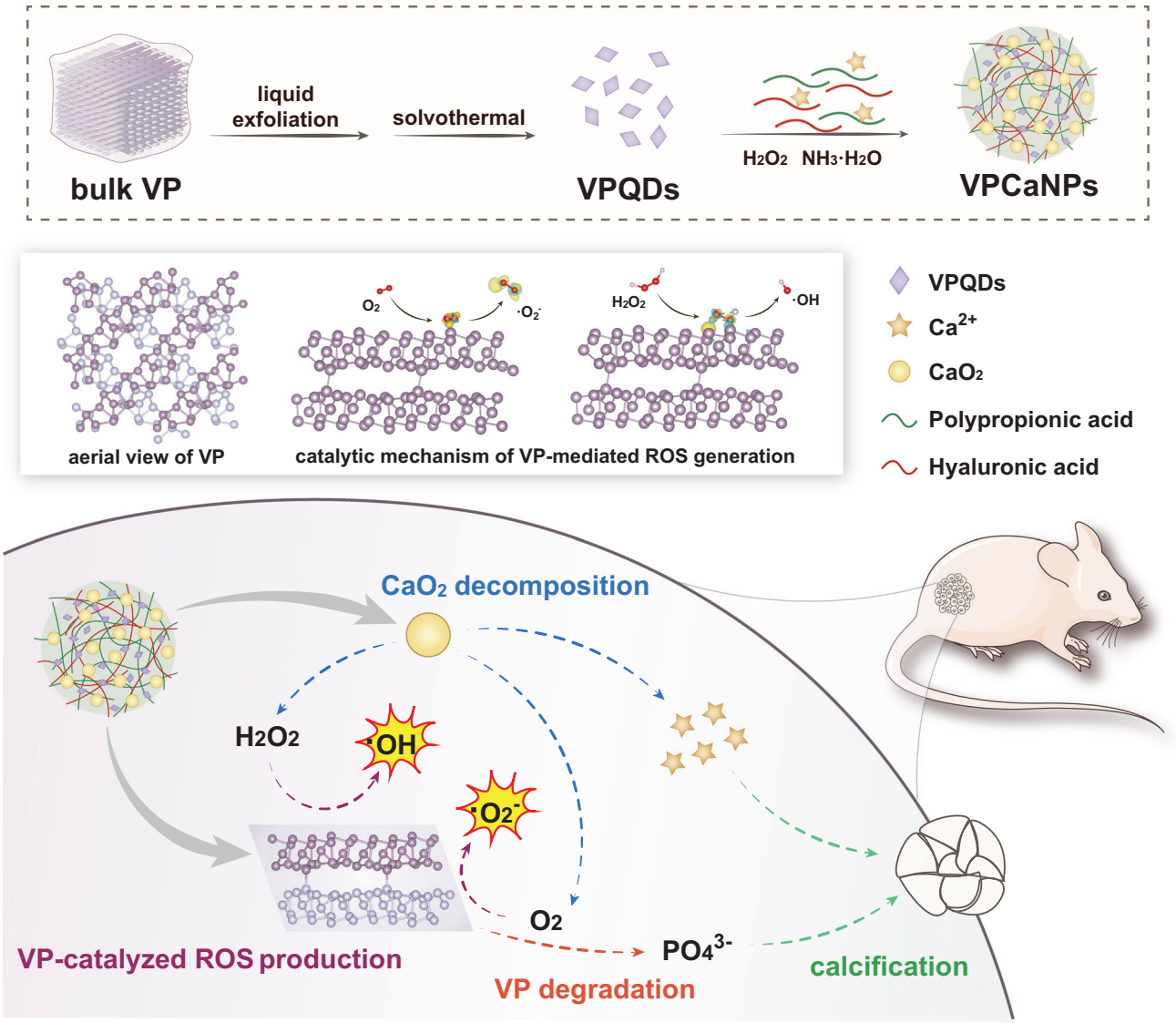

Fig. 1 | Schematic illustration of the preparation and antitumor mechanism of VPCaNPs. The preparation of VPCaNPs contains the top-down synthesis of VPQDs and the one-pot fabrication of VPCaNPs. The antitumor properties are based on the fate of VPCaNPs, including the release of cargos, CaO_2 decomposition, VP-catalyzed ROS generation, O_2-mediated VP degradation, and calcifation.

(E_{NHE}) is set to −4.44 eV with respect to absolute vacuum scale (E_{AVS} = 0) as a reference[28] in Fig. 3g. The potential of E_{CB} (vs NHE) is higher than the redox potential for O_2(aq.)/$\cdot O_2^-$ of −0.16 eV[29], indicating energetically possibility for $\cdot O_2^-$ formation. DFT calculations were also performed to predict the catalytic properties of VP. A 2 × 2 × 1 VP supercell, which consists of 168 phosphorus atoms, was established and adopted in all the calculations in this work. As descried in Fig. 2b, the calculated lattice constants of 2 × 2 × 1 pristine VP supercell are a = 18.41 Å and b = 18.29 Å, respectively. As shown in (Supplementary Fig. 6), VP is a semiconductor with a calculated direct E_g of 1.73 eV using generalized gradient approximation with Perdew-Burke-Ernzerhof (GGA-PBE) functional. From orbital-resolved electronic density of states (DOS) analysis, the E_{CB} is contributed by both s and p orbitals of phosphorus atoms, while the E_{VB} is mainly contributed by the p orbitals. The calculated lattice constants, bandgap and DOS properties are consistent with the previous reports[22,30,31], affirming the appropriateness of the structural model, calculation method and parameters employed. The E_{CB} of −0.43 eV and the E_{VB} of 1.29 eV are both located at high symmetric point Γ in the first Brillouin zone. The computational simulation E_g (1.73 eV) is larger than the laboratory one (1.64 eV), but the potential of E_{CB} (vs. NHE) is also higher than the redox potential for O_2(aq.)/$\cdot O_2^-$ of −0.16 eV, indicating energetically possibility for $\cdot O_2^-$ formation catalyzed by VPQDs, the same conclusion as derived from laboratory band structure.

To further understand the catalytic mechanism of VP-mediated $\cdot O_2^-$ generation, Gibbs free energy difference (ΔG) calculations and charge transfer analysis were performed as shown in Fig. 3h, i, respectively. ΔG adopted to estimate the catalytic activity has the following expression,

$$\Delta G = \Delta E + \Delta E_{ZPE} - T\Delta S, \quad (1)$$

where ΔE, ΔE_{ZPE}, and ΔS represents the difference of electronic energy, the zero-point energy, and the entropy, respectively. T represents the human body temperature (310.15 K). The zero-point energy was determined through vibration frequency simulations, where the adsorbate molecule remained unrestricted in its movement, while the substrate remained fixed due to its minimal vibration. After a O_2 molecule contacted and adsorbed on the surface of VP, electrons tend to transfer from VP to O_2 with a low ΔG of 0.36 eV. It is reasonable because the O sp hybrid orbital in O_2 is electron-deficient, while the P sp^3 hybrid orbital contains a pair of unbounded electrons, allowing VP

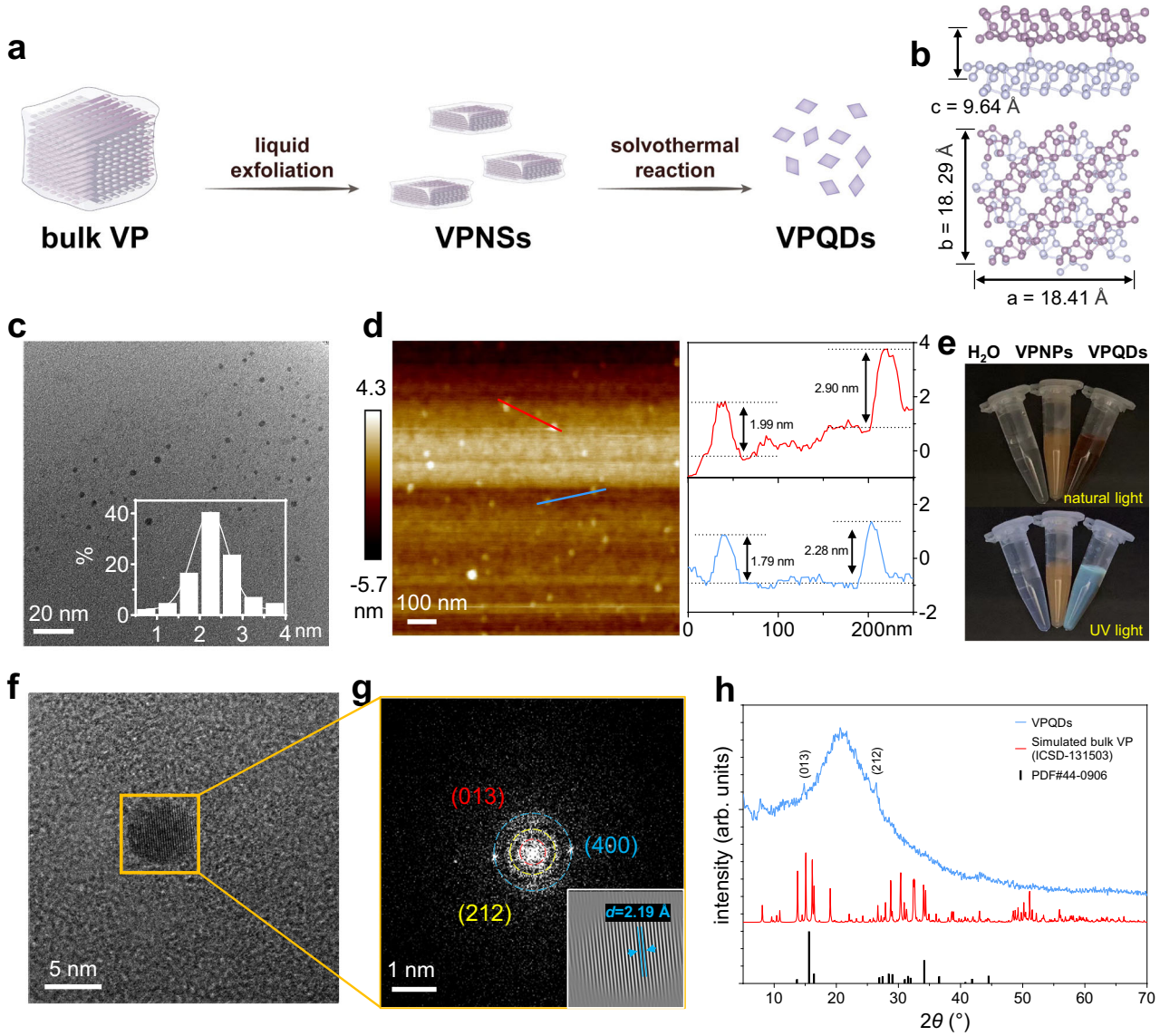

Fig. 2 | Characterization of VPQDs. a Simplified steps for VPQDs synthesis. **b** Simulated VP with side and aerial views. **c** TEM image of VPQDs. Insert: size distribution of VPQDs. **d** AFM image of VPQDs and height of VPQDs corresponding to marked lines. **e** Photographs of water, VPNSs, and VPQDs under natural light and ultraviolet light. **f** HRTEM image of VPQDs. **g** Corresponding FFT image of VPQDs in (**f**). Blue, yellow, and red circles represent (400), (212), and (013) planes, respectively. Insert: inverse FFT image of the lightest point at (400) planes. **h** XRD spectrum of VPQDs, simulated bulk VP, and the powder diffraction file of VP (PDF#44-0906). Each experiment was repeated three times independently with similar results.

to drive O_2 reduction as an electron donor. As a consequence, excited-state electrons at CB of VP tend to transfer to the electronic orbitals of O_2, and then·O_2^- could be desorption and released after overcoming 0.93 eV energy barrier.

Since ·OH are also a common therapeutic active molecule for tumor catalytic strategy and ·OH was detected in vitro, the possibility of VP-mediated ·OH production was also investigated. In general, ·OH can be derived from either H_2O or H_2O_2[32,33]. Therefore, two possible reaction pathways starting from H_2O and Fenton-like pathway starting from H_2O_2, respectively, are listed below[34–36],

$$* + H_2O/H_2O_2 \rightarrow *H_2O/*H_2O_2, \quad (2)$$

$$*H_2O \rightarrow *H + \cdot OH, \quad (3)$$

$$*H_2O \rightarrow *OH + H^+ + e^-, \quad (4)$$

$$*OH \rightarrow * + \cdot OH, \quad (5)$$

$$*H_2O_2 \rightarrow *OH + \cdot OH, \quad (6)$$

where * represents an adsorption site of VP. $*H_2O$,$*H_2O_2$, *H and *OH represent VP adsorbed with H_2O, H_2O_2, H and ·OH, respectively. For simplicity of calculation, H^+–e^- ion pair is treated as 1/2 H_2. As shown in Fig. 3j, the ΔG values for H_2O and H_2O_2 molecule adsorption on VP are both 0.24 eV, implying that both H_2O and H_2O_2 molecules exhibit the tendency to adsorb onto the surface of VP (Eq. (2)), providing a prerequisite for catalytic reaction. After H_2O adsorption, one of the H–O bond in the H_2O is broken and divided into adsorbed H (H*) and adsorbed OH (*OH). Therefore, subsequent reactions may occur via two different pathways. One is that, as listed in Eq. (3), the *OH desorbs from VP and one ·OH releases with an extremely high ΔG value of 4.28 eV. The other is going through Eqs. (4) and (5) successively, that is, VP first catalyzes one H_2O molecule to generate one *OH and one H^+–e^-

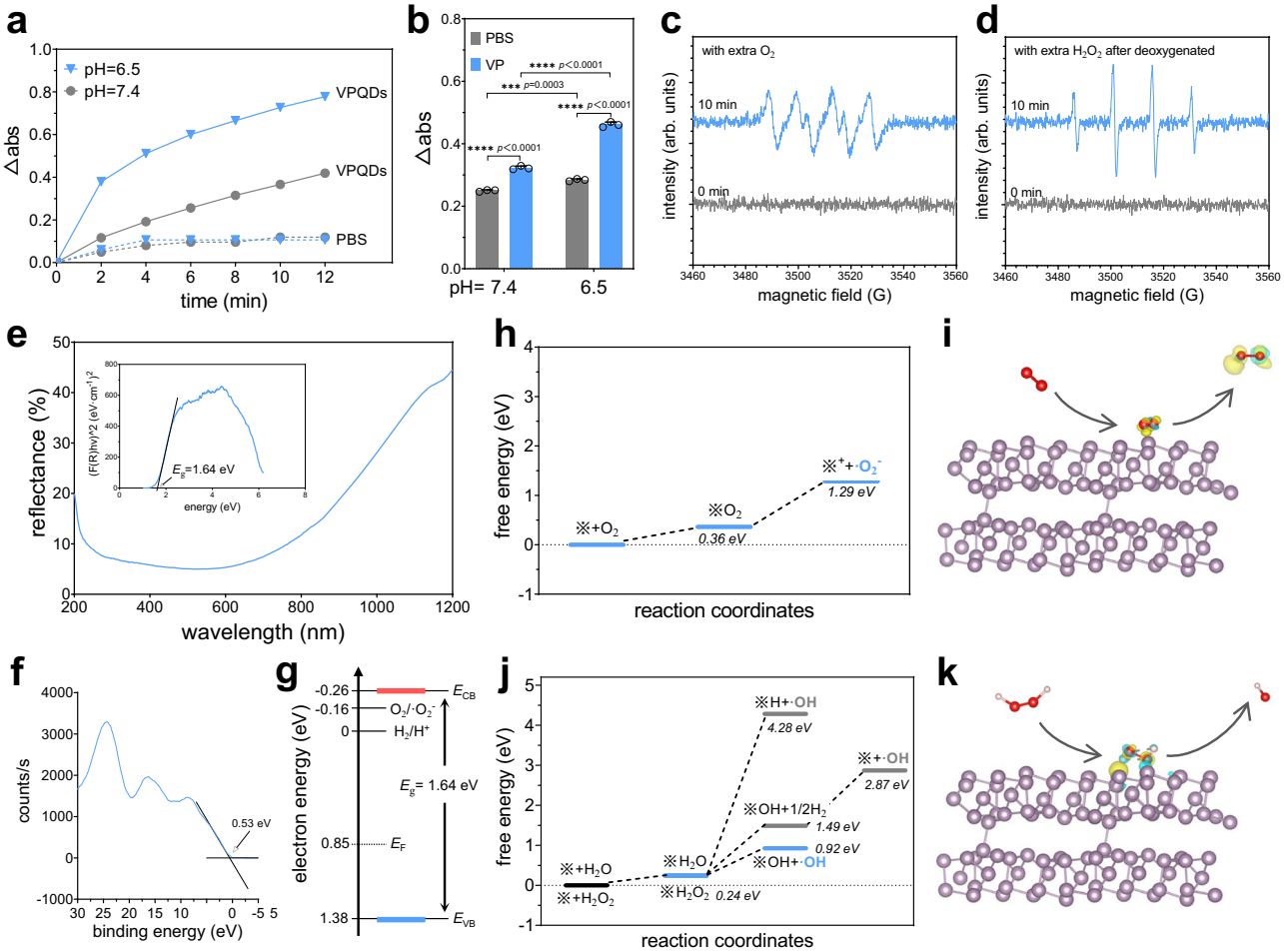

Fig. 3 | VP's catalytic efficacy to generate $\cdot O_2^-$ and ·OH. VPQDs-mediated DPBF decrease in (**a**) the oxygenated condition and (**b**) the H_2O_2-sufficient condition at different pH. Data in (**b**) are presented as the mean with SD ($n = 3$ independent samples). Statistical differences were analyzed by a two-way ANOVA with Tukey's multiple comparisons test. The PBS groups were control groups. ESR results of VPQDs in (**c**) the oxygenated condition and (**d**) the H_2O_2-sufficient condition. **e** UV-vis diffuse reflection spectrum (DRS) of lyophilized VPQDs powder. Insert: corresponding Tauc plot of DRS plot according to Kubelka-Munk formula: $(F(R)h\nu)^2 = k/s = (1\text{-}R)^2/2R = B(h\nu\text{-}E_g)$, where $(F(R)h\nu)^2$ as y axis, $h\nu$ as x axis. **f** Valence band spectra of lyophilized VPQDs powder. **g** Simplified band structure vs. NHE of VPQDs. **h** Calculated ΔG of VP-mediated $\cdot O_2^-$ generation. **i** Charge density difference profiles for the adsorption of O_2 molecule on VP. Smooth yellow and blue shading illustrate the charge-accumulation and charge-depletion, respectively. **j** Calculated ΔG of VP-mediated ·OH generation. **k** Charge density difference profiles for the adsorption of H_2O_2 molecule on VP. Smooth yellow and blue shading illustrate the charge-accumulation and charge-depletion, respectively.

ion pair, and then one ·OH generates through desorption. The ΔG of the two steps in this pathway is 1.49 eV and 2.87 eV, respectively. Notably, the VP-mediated Fenton-like reaction with H_2O_2 as the catalytic substrate generates ·OH required only one step (Eq. (6)) with the lowest ΔG value of 0.92 eV. The mechanism is that, as shown in Fig. 3k, the unbounded electron pairs in P sp^3 hybrid orbitals allow VP to act as an electron donor like Fe^{2+} in Fenton (Fenton-like) reactions[19]. Mediated by electron transfer from VP to O atom, the orbital overlap between the two O atoms in H_2O_2 is weakened, leading to homolytic cleavage of the O–O bond and generating ·OH eventually. Therefore, VP has much more tendency to catalyze ·OH generation via Fenton-like pathway. In summary, the calculation results explained that VP is a potential catalyst candidate for ROS ($\cdot O_2^-$ and ·OH) generation.

Fabrication and characterization of VPCaNPs

Given the hypoxic microenvironment and insufficient supply of H_2O_2 in tumor tissues, CaO_2 was chosen as a substrate donator for VPQDs due to its generation ability of both O_2 and H_2O_2. HA and PAA were chosen as carriers due to the biocompatibility. HA can target CD44 on the surface of tumor cells and induce nanoparticle endocytosis followed by decomposed with overexpressed hyaluronidase[37], leading to nanoparticle collapse. As pH decrease, PAA will absorb H_2O and swell, which promote the release of cargos[38]. Importantly, carboxyl groups of PAA and HA can bind with Ca^{2+} for nucleation and steric hindrance can inhibit agglomeration of nanoparticles[39]. By adding H_2O_2 and $NH_3{\cdot}H_2O$ into a mixture of HA, PAA, Ca^{2+}, and VPQDs in methanol solution, VPCaNPs containing both VPQDs and CaO_2 were prepared via a one-pot method (Fig. 4a). In detail, HA, PAA, $CaCl_2$, and VPQDs were added into methanol solution. After thoroughly mix, the solution was transfered to an ice, ultrasonic bath. Next, H_2O_2 was added dropwise, and $NH_3{\cdot}H_2O$ was introduced into the system quickly. Finally, nanoparticles were collected by centrifugation. Nanoparticles prepared without VPQDs are termed as CaNPs.

Several tools were applied to confirm the successful synthesis of VPCaNPs. Figure 4b showed that VPCaNPs are small nanoparticles with a size of 30 nm around. And the zeta potential was quantitatively analyzed as approximately −30 mV (Supplementary Fig. 7). Scanning electron microscope image and energy dispersive spectrometry mapping (Fig. 4c) exhibited a homogeneous P, Ca, O, and C distribution in VPCaNPs and corresponding elemental distribution spectrum was shown in supplementary Fig. 8. In Fourier transform infrared (FT-IR) spectrum (Fig. 4d), the characteristic peaks of VP, CaO_2, and

https://doi.org/10.1038/s41467-024-50769-0

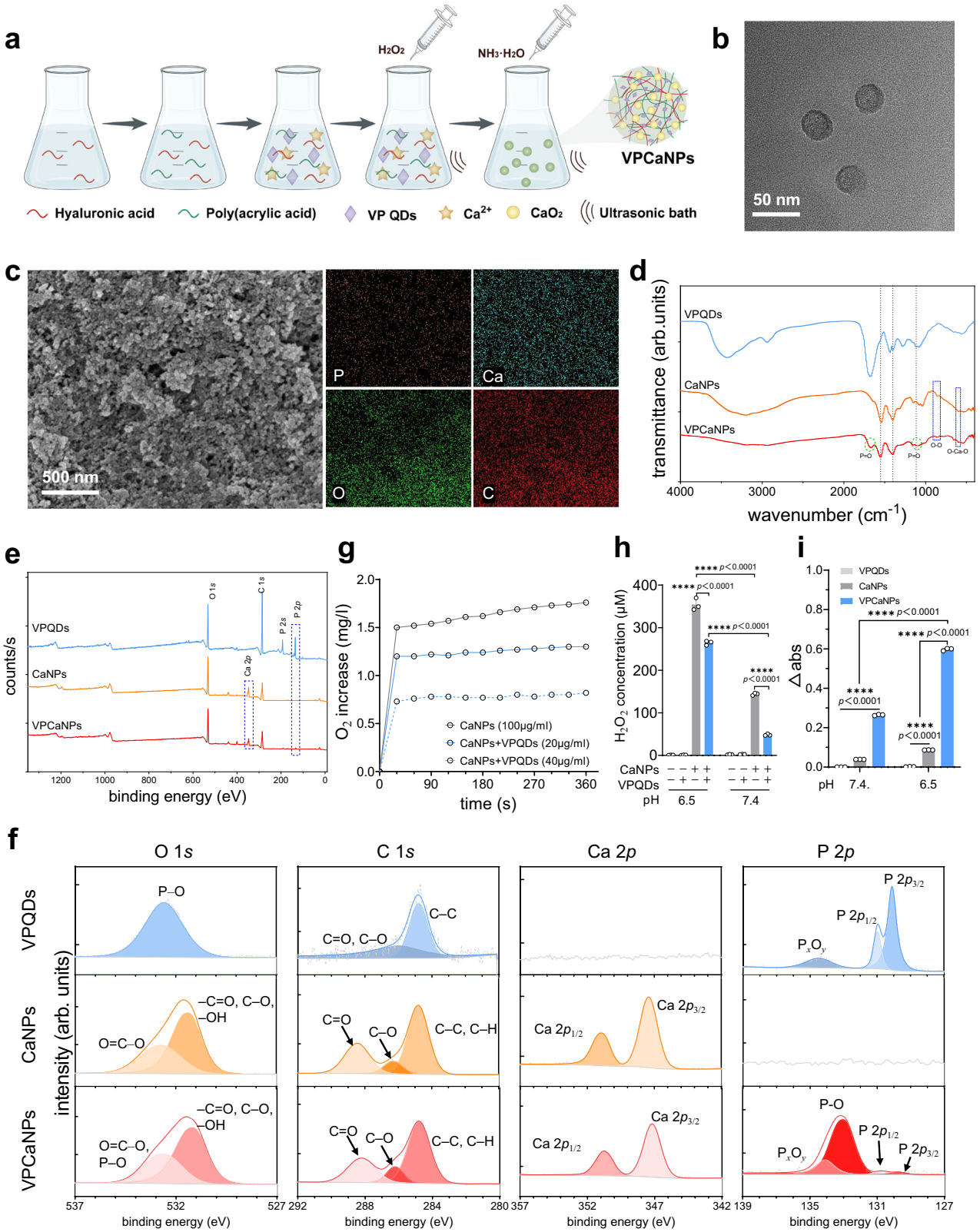

Fig. 4 | Synthesis and characterization of VPCaNPs. a Synthesis of VPCaNPs. **b** TEM image of VPCaNPs. **c** SEM and EDS mapping of VPCaNPs. TEM and SEM experiments were repeated three times independently with similar results. **d** FT-IR spectrum and (**e**) XPS survey spectrum of VPQDs, CaNPs, and VPCaNPs. **f** Fine scan XPS of O 1*s*, C 1*s*, Ca 2*p*, and P 2*p*. **g** Oxygen increase in 4% FBS containing CaNPs and different concentrations of VPQDs at the pH of 6.5. **h** H_2O_2 concentration in 4% FBS containing CaNPs and different concentrations of VPQDs at the pH of 6.5 and 7.4. **i** Absorbance decrease of DPBF in 4% FBS containing VPCaNPs at different pH. Data in (**h**, **i**) are presented as the mean with SD ($n = 3$ independent samples). Statistical differences were analyzed by a two-way ANOVA with Tukey's multiple comparisons test.

polymers were exhibited. The FT-IR peak at 1668 cm^{-1} is attributed to the bending vibrations of P = O bond. And the signals in the range of 1000 to 1100 cm^{-1} is contributed by the stretching vibration of P = O bond[23]. The peak around 861 cm^{-1} corresponded to the O–O bridge of CaO_2. Additionally, the slight peak at 595 cm^{-1} was attributed to O–Ca–O vibrations[40,41]. And the strong peaks at 1400 and 1550 cm^{-1} can be attributed to stretching vibrations of carboxylate groups in polymers. According to XPS spectrum in Fig. 4e, VPCaNPs shared the characteristic peaks of P 2*p* (~133 eV) with VPQDs and Ca 2*p* (~347 eV) with CaNPs, indicating successful integration of CaO_2 and VPQDs into VPCaNPs. Most signals at O 1*s* and C 1*s* of CaNPs and VPCaNPs can be ascribed to polymers. Atomic concentrations of these peaks were measured and showed in supplementary Table 1. The high-resolution scans of four elements revealed more information (Fig. 4f). In VPQDs, the crystalline P (P $2p_{1/2}$ at 130.9 eV, P $2p_{3/2}$ at 130.1 eV) occupied most proportion of P 2*p* and oxidation state (wide peak around 134.5 eV) took a small area, while one peak at the binding energy of 532.6 eV attributing to the O atoms in P–O bonds, indicating inevitable slight oxidation of VPQDs during synthesis. The signal from C 1*s* of VPQDs could be attributed to additional C used for locating, i.e., carbon contaminant. O 1*s* spectrum can be explained as adsorbed oxygen and partially oxygenated VPQDs. Because polymers (HA and PAA) made up most of CaNPs and VPCaNPs, the peaks in the O 1*s* region of CaNPs and VPCaNPs at binding energy of 532.8 eV was attributed to O=C–O and 531.4 eV could be ascribed to –C=O, C–O, or –OH groups. The three main peaks in the C 1*s* region were assigned to C=O at 288.5 eV, C–O at 286.3 eV, and C–C or C–H at 284.8 eV. Ca 2*p* signal was a result of CaO_2 synthesis. Compared with VPQDs, the new peak at 133.2 eV gave a clue that VPQDs bound with electronegative oxygen (in HA, PAA, and CaO_2)[42–46].

Next, we assessed the ability of CaNPs to produce oxygen by dispersing CaNPs in 4% fetal bovine serum (FBS) with different pH and recorded the oxygen content of the solution with a dissolved oxygen analyzer. As shown in supplementary Fig. 9, O_2 concentration of CaNPs groups surged in the first 60 s, and after 90 s, CaNPs releases oxygen at a relative constant rate. In acidic conditions, oxygen release rates increase, implying that acidic tumor environments are preferable for oxygen delivery. This result also implied that VPQDs can consume dissolved O_2 and acidic condition promote the reaction. Also, in the presence of VPQDs, the dissolved oxygen content of CaNPs showed slower growth, while exhibiting a dependence on the concentration of VPQDs, implying that VPQDs acted as oxygen consumers of CaNPs (Fig. 4g). Similarly, we mixed CaNPs and VPQDs to measure H_2O_2 production by CaNPs and its consumption by VPQDs. H_2O_2 content was quantified via a ferric-xylenol orange method. As shown in Fig. 4h, the presence of VPQDs can reduce the amount of H_2O_2 produced by CaNPs. This can be attributed to the catalytic consumption of VPQDs towards O_2 and H_2O_2, which leads to the generation of ROS. To further assess whether the fabrication of VPCaNPs would attenuate the inherent acid-response catalytic activity of VPQDs, DPBF was applied as a ROS probe to detect the VPCaNPs mediated generation of total ROS in FBS at different pH level. The absorbance at 425 nm was recorded at the initial and 10 min post reaction. As shown in Fig. 3i, compared to pH at 7.4, the consumption of DPBF in acidic conditions (pH at 6.5) was significantly increased, implying that the acid-promoting catalytic properties of VPQDs were maintained in as-prepared VPCaNPs, which makes its potential for further application in tumor catalytic therapy.

In vitro antitumor effects and biocompatibility of the acid-sensitive catalytic system

According to promising catalytic results in solutions, the catalytic performance and antitumor effect of VPCaNPs on cells were then investigated. Firstly, the biocompatibility of different nanoparticles (VPQDs, CaNPs, and VPCaNPs) with normal cells were evaluated through cell counting kit-8 (CCK-8) assay to ensure the biosafety. As shown in supplementary Fig. 10, none of the three nanomaterials exhibits significant cytotoxicity to mouse fibroblasts cells (L929) and human embryonic kidney cells (HEK293T). These results can be interpreted as (1) protective effect of acid-sensitive polymers PAA, (2) less targeting of nanoparticles due to less CD44-expressed on the cell surface, (3) insufficient catalytic substrates for VPQDs in non-malignancy cells, (4) lower catalytic efficacy of VPQDs in neutral than acidic conditions, indicating great potential for clinical transformation. Further, the cytotoxicity of three nanomaterials toward breast cancer cells (4T1) were evaluated. As shown in Fig. 5a, the introduction of CaO_2 significantly increased the cytotoxicity of VPQDs. It can be attributed to rapid hydrolysis of CaO_2 generates three important substances: H_2O_2, O_2, and Ca^{2+}, among which H_2O_2 and O_2 are substrates of VPQDs to generate highly-active and poisonous radicals, and Ca^{2+}-overload could promote ROS-induced cell death and calcification.

To verify the hypothesis above, we investigated the uptake time of VPCaNPs by 4T1 cells using fluorescent dye sulfo-cyanine5 (cy5) as an indicator. Specifically, cy5 was added into the mixture of VPQDs, Ca^{2+}, HA and PAA during the synthesis process of VPCaNPs, and the collected cy5-VPCaNPs were incubated with 4T1 cells for different time for flow cytometry. As shown in Fig. 5b, fluorescent intensity of cy5 reached its peak after 4 h of co-incubation and remained relatively stable over time. The images of 4 h-incubation 4T1 cells were taken using a confocal microscope, indicating that VPCaNPs were ingested successfully into cells rather than stacking on the cell membrane (Fig. 5c). The uptake of VPCaNPs can be mediated through the binding of HA towards CD44 receptor and the overexpressed hyaluronidase in tumor cells can induce nanoparticle collapse through HA degradation[37]. Next, nanomaterial mediated intracellular ROS generation were investigated by a nonspecific probe, DCFH-DA. As shown in Fig. 5d, a mild ROS accumulation was observed after treatment with VPQDs alone, which was caused by the lack of catalytic substrates in cells, while treatment with CaNPs showed a larger increase in fluorescence intensity, which was a result of a self-amplifying loop of Ca^{2+} and H_2O_2[41]. VPQDs could further catalyze the decomposition products H_2O_2 and O_2 of CaO_2 into ·OH and $\cdot O_2^-$, respectively. Therefore, the VPCaNPs treatment group showed the strongest ROS intensity, indicating the highest catalytic efficacy. Further, specific probes were adopted to pinpoint the source of ROS. After loading probes, cells were separately incubated with saline, VPQDs, CaNPs, and VPCaNPs for 6 h and then collected for flow cytometry. As shown in Fig. 5e, the fluorescence intensity of the oxygen sensor, $[Ru(dpp)_3]Cl_2$ decreased significantly in cells incubated with CaNPs or VPCaNPs, proving the intracellular O_2 generation capacity of CaO_2. After VPQDs introduction into VPCaNPs, part of CaO_2-generated O_2 was consumed as the catalytic substrates for producing $\cdot O_2^-$ (Fig. 5f). The result also explains why, in Fig. 4e, the probe's fluorescence intensity after CaNPs treatment was reduced more significantly than that in the VPCaNPs group. A $\cdot O_2^-$ positive signal of VPQDs meant that a small amount of O in the culture medium was catalyzed into superoxide radicals and that of CaNPs can be ascribed to Ca^{2+} accumulation stimulated-NADPH oxidase activity and electron transport chain leakage[47]. Regarding H_2O_2 (Fig. 5g), the H_2O_2 signal peak was significantly positive-shift after CaNPs or VPCaNPs treatment, indicating that CaO_2 has the ability to release H_2O_2 intracellular. VPCaNPs treatment could produce more H_2O_2, which may be contributed to the superoxide dismutase (SOD) mediated $\cdot O_2^-$ conversion into H_2O_2 in tumor cells[1]. In addition, H_2O_2 can also decompose into ·OH with $\cdot O_2^-$[48]. Therefore, CaNPs showed the ability to produce small amounts of ·OH and VPCaNPs group exhibited the most ·OH signal, which was catalyzed by VPQDs (Fig. 5h). Previous studies have proved that CaO_2 induced calcium-overload and oxidative stress can trigger mitochondrial permeability transition pore opening, leading to the loss of mitochondrial membrane potential[49]. Inspired by that, we choose JC-1 as the mitochondrial membrane potential probes due to the potential-dependent accumulation in

https://doi.org/10.1038/s41467-024-50769-0

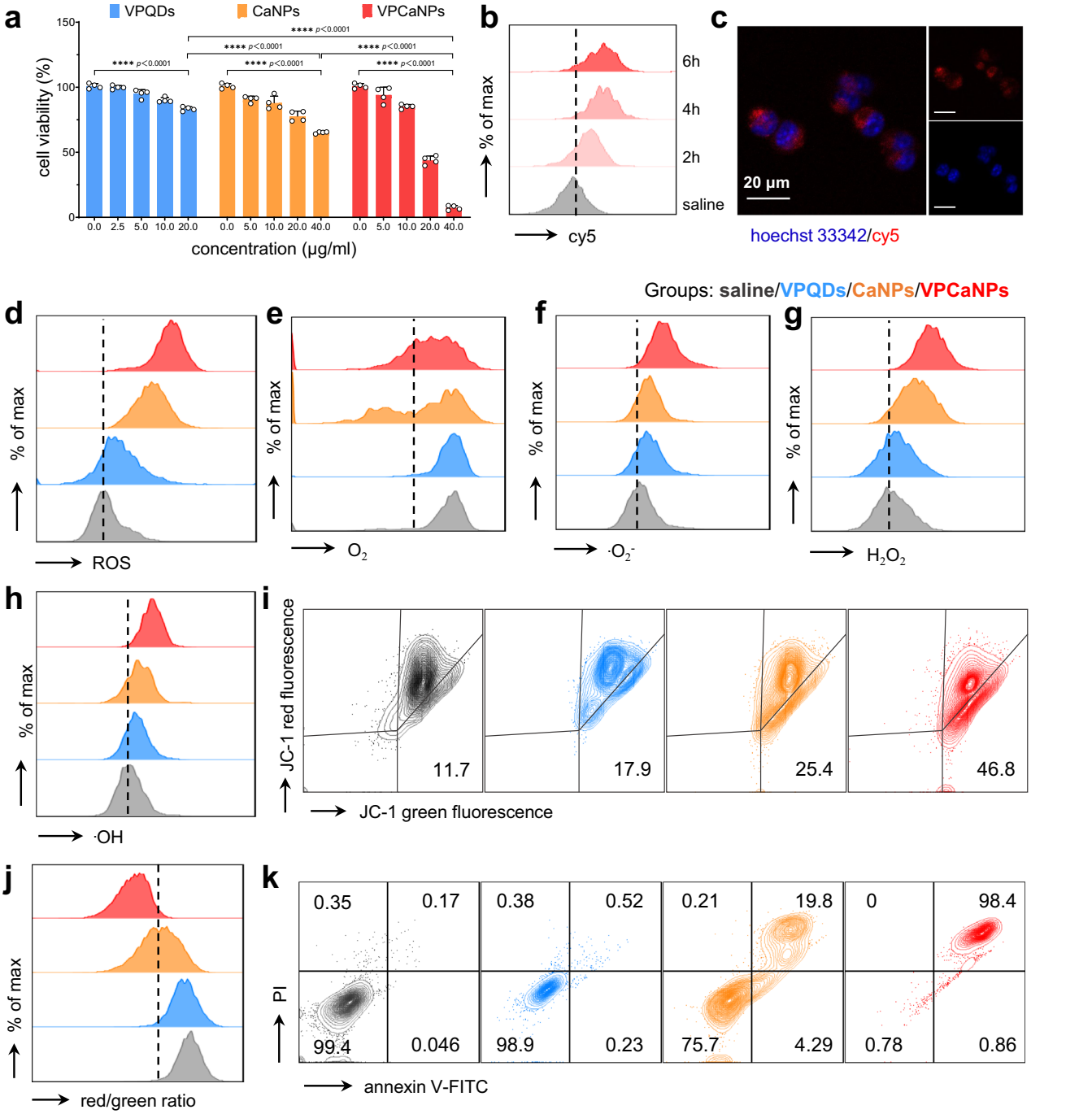

Fig. 5 | Catalytic activity and cytotoxicity of VPCaNPs. a Cell viability of VPQDs, CaNPs, and VPCaNPs by cck8 assays. Data are presented as the mean with SD ($n = 4$ biologically independent cells). Statistical differences were analyzed by a two-way ANOVA with Tukey's multiple comparisons test. **b** Representative fluorescence quantification of intracellular cy5-labled VPCaNPs with different incubation time. **c** Representative fluorescence image of 4T1 cells incubation with cy5-labeled VPCaNPs for 4 h. This experiment was repeated three times independently with similar results. Representative fluorescence quantification of intracellular level of (**d**) ROS, (**e**) O_2, (**f**) $\cdot O_2^-$, (**g**) H_2O_2, and (**h**) ·OH of 4T1 cells incubation with saline, VPQDs, CaNPs, and VPCaNPs for 6 h by FCM. Representative FCM images of (**i**) JC−1, (**j**) red/green ratio of lipid peroxidation probe, C11-BODIPY(581/589), and (**k**) PI and annexin V-FITC of 4T1 cells incubation with saline, VPQDs, CaNPs, and VPCaNPs for 12 h. The saline groups were control groups. Each experiment was repeated three times independently with similar results.

mitochondria. As shown in Fig. 5i, VPCaNPs treatment showed most decrease of red fluorescence (J-aggregates), indicating most depolarization of membrane potential. Lipid peroxidation is another hallmark of oxidative stress-induced cell death, which can be initiated by ·OH through attacking polyunsaturated acyl chains[50]. C11-BODIPY$^{581/591}$ is loaded with 4T1 cells to measure lipid peroxidation after nanomaterials incubation. The increase of green fluorescence signal and decrease of red fluorescence signal means the probes were attacked by oxidative radicals, and VPCaNPs induced the most significant reduction of the red/green ratio of fluorescence signal (Fig. 5j). Consequently, these phenomenon also supports the results of the highest apoptosis rate of cells treated with VPCaNPs (Fig. 5k).

Calcification of tumor cells after nanosystem decomposition

Tumor calcification can be associated with a good prognosis in clinical practice, and previous studies have reported that artificially inducing

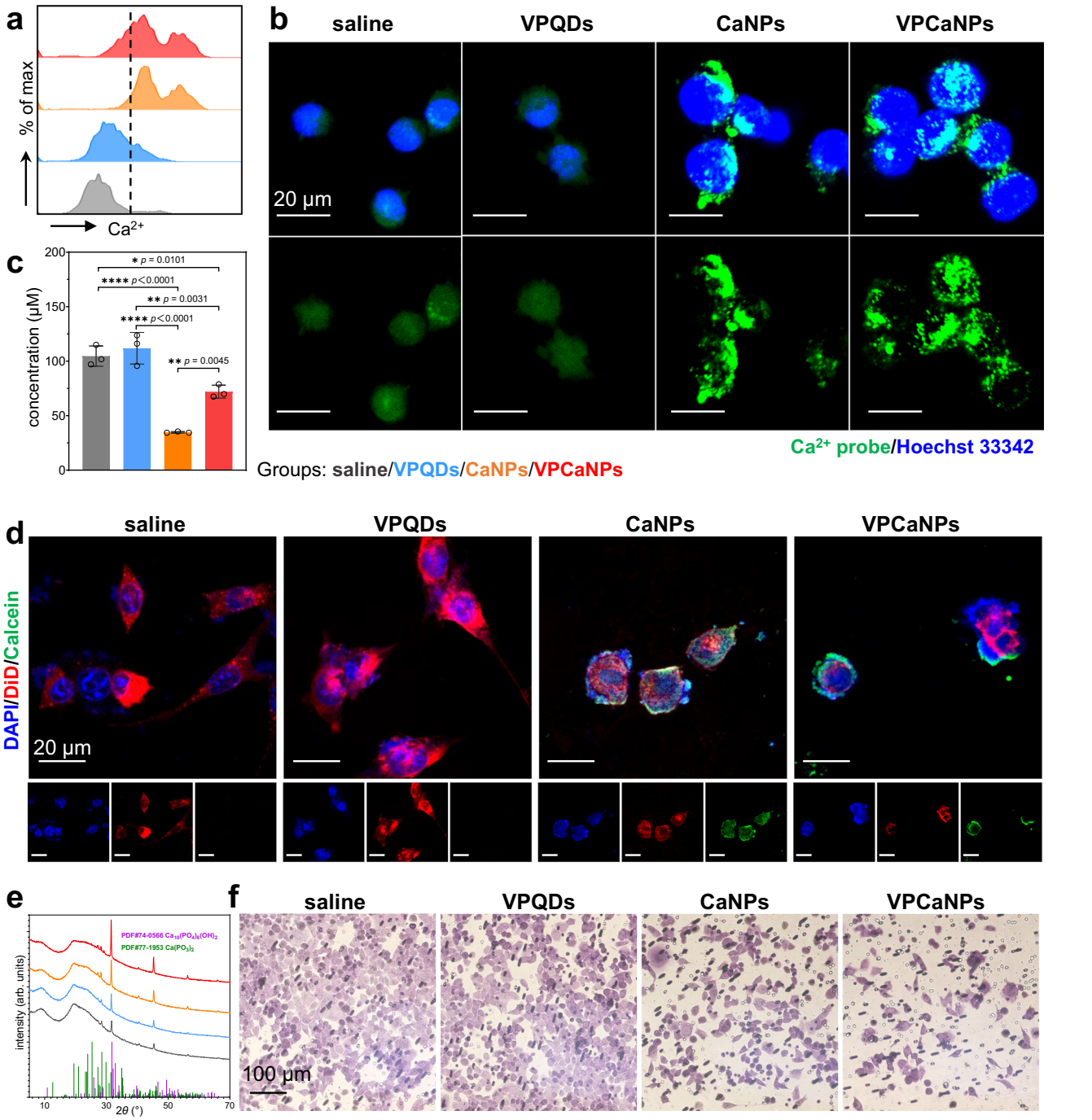

Fig. 6 | Calcification of tumor cells after incubation with VPCaNPs. Representative fluorescence quantification of intracellular Ca^{2+} by (**a**) FCM and (**b**) CLSM after incubation with saline, VPQDs, CaNPs, and VPCaNPs for 4 h. Scale bar = 20 μm. **c** Intracellular phosphorous concentration after incubation for 24 h. Data are presented as the mean with SD ($n = 3$ biologically independent cells). Statistical differences were analyzed by a two-way ANOVA with Tukey's multiple comparisons test. **d** Cell calcification after incubation with nanomaterials for 48 h. **e** XRD pattern of the collected products from cell exocytosis after treatment with saline, VPQDs, CaNPs, and VPCaNPs for 48 h. **f** Representative images of transwell cell migration assay with saline, VPQDs, CaNPs, and VPCaNPs incubation. Scale bar = 100 μm. The saline groups were control groups. Each experiment was repeated three times independently with similar results.

tumor calcification can inhibit tumor growth[51,52]. The formation of hydroxyapatite, the main chemical component of calcification points, required calcium and phosphate ions, both of which can be generated after VPCaNPs degradation. Also, great number of carboxylate groups from the carriers (HA and PAA) of as-prepared nanomaterials can chelate calcium ions and trigger in situ calcium phosphate deposition[53]. We incubated 4T1 cells with different nanomaterials for 4 h, and then verified that both CaNPs and VPCaNPs could significantly increase the intracellular calcium ion concentration by flow cytometry (Fig. 6a) and confocal microscopy (Fig. 6b). In addition, after 5 days dispersed in PBS with different condition, the absorbance decrease of VPQDs in oxygenated condition increased significantly, and the pH did not have much effect (Supplementary Fig. 11a). The dramatical increase of phosphate concentration in oxygenated 4% FBS was also observed (Supplementary Fig. 11b). The results proved that VPQDs can be slowly degraded in an oxygen-rich environment, though VP is the most thermodynamically stable allotrope reported so far[22]. Intracellular phosphate concentrations were measured 24 h post nanomaterials incubation as well

(Fig. 6c). There was no significant difference between saline and VPQDs groups due to no extra oxygen. CaNPs group showed the lowest phosphate concentration because phosphate can be precipitated with Ca^{2+}. The rise of concentration in VPCaNPs incubated cells than CaNPs can be ascribed to O_2-mediated VPQDs degradation. After different nanoparticles were incubated with the cells for 48 h, calcification on the plasma membrane was observed in both CaNPs and VPCaNPs groups (Fig. 6d). Minerals were collected and their components were identified by XRD (Fig. 6e). The results show that CaNPs and VPCaNPs can significantly lead to the formation of hydroxyapatite (PDF#74-0566, purple line) and calcium phosphate (PDF#77-1953, green line). In addition, cell migration experiments with different nanoparticles at low concentrations were conducted and the conclusion was consistent with the above results that CaNPs and VPCaNPs could reduce cell migration the most (Fig. 6f and supplementary Fig. 12).

In vivo distribution, antitumor effect and tumor calcification

Encouraged by the promising outcomes of in vitro experiments (including catalytic ability, degradation, calcification, as well as selective killing effect), in vivo tumor therapy using VPCaNPs was subsequently initiated. Prior to systematic administration test, we assessed the anti-tumor effect intratumorally. 4T1 tumor-bearing mice were randomly divided into 4 groups with different intravenous treatments: saline (group 1), VPQDs (group 2), CaNPs (group 3), and VPQDs+CaNPs (group 4). Until the tumor volume reached to 60 mm^3, the dose of P and Ca were 4.5 and 10 mg/kg, respectively. As shown in Supplementary Figs. 13a, b, tumor volume of mice in group 4 showed the least increase. After 14 days treatment, tumors were excised from euthanized mice and stained with alizarin red. As depicted in Supplementary Fig. 13c, tumor sections in groups 3 and 4 displayed significant dark red staining, indicating tumor tissue calcification due to CaO_2.

The superior therapeutic efficacy and notable calcification achieved by VPCaNPs intratumoral administration instill confidence in the systemic drug delivery. Cy5-labeled VPCaNPs were used to measure in vivo distribution and tumor accumulation before assessing the efficacy of systemic delivery. 4T1 xenograft tumor mice were *i.v.* administrated with cy5-VPCaNPs and the main organs and tumors were dissected for fluorescence imaging 24 h or 48 h post injection. As shown in Fig. 7a, b, nanoparticles could accumulate in tumor tissues for at least 48 h, which ascribed to the tumor targeting property of HA and EPR effect. Also, nanoparticles could accumulate in metabolic organs (liver, spleen, and kidney) to be excreted from the body. The highest fluorescence intensity of lungs could be attributed to the small size of VPCaNPs to penetrate through pulmonary capillaries and the nanoparticle-captured alveolar macrophages[54]. Next, 4T1 tumor-bearing animals were randomly divided into four groups for tail vein injection: saline (group 1), VPQDs (group 2), CaNPs (group 3), and VPCaNPs (group 4). As anticipated, VPCaNPs showed significant antitumor effects following a single intravenous dose (Fig. 7c, d). After 14 days of administration, all mice were euthanized and the tumors were sectioned for TUNEL staining and alizarin red staining. Figure 7e shows that the tumors in the VPCaNPs group were characterized with significant green fluorescence of fitc-dUTP, indicating tumor cell apoptosis. Additionally, the formation of red calcification points of group 3 and 4 was evident on alizarin red stained sections (Fig. 7f). Representative H&E staining slides revealed that the lungs of mice in the saline group exhibited evidently vascular tumor metastasis with inflammatory cell infiltration, whereas normal alveolar structure was observed in the group 4, indicating that VPCaNPs can mitigate tumor metastasis to a certain extent (Fig. 7i).

In vivo immune activation after VPCaNPs systematic administration

The immune level will affect the therapeutic outcome and progression of cancer patients. In addition to directly killing malignant cells, indirectly eliminating tumors by activating immunity is another choice[55]. ROS production is essential in immunogenic cell death of cancer cells[56] and Ca^{2+} can regulate the activation of several immune cells including T cells, natural killer (NK) cells, and dendritic cells (DCs)[57]. Therefore, we investigated the immune activation ability of VPCaNPs, both ROS generators and Ca^{2+} donors. Cells from the draining lymph nodes were collected 14 days post different treatments. Among them, the DCs was labeled with surface antibodies of CD45 and CD11c, and the mature and activated DCs were labeled with antibodies of CD80 and I-A^b (a type of major histocompatibility complex II), respectively. Obvious increase in $CD80^+$ and I-A^{b+} DCs ($CD45^+CD11c^+$) can be attributed to enhanced exposure of tumor antigens induced by VPCaNPs-mediated ROS amplification (Fig. 8a, b). Following the maturation of DCs, the main antigen presenting cells (APCs), T cells can be activated. Tumor-infiltrating cytotoxic T lymphocyte (CTLs, $CD45^+CD3^+CD8^+$) can be activated by both APCs and tumor cells followed by direct killing tumors with perforin, granzymes, or receptor-ligand engagement (FAS or TRAIL) or secreting high-level tumor-killing cytokines to indirect influence tumor fate[58]. A slight increase in $CD8^+$ T cells was observed in tumor tissues of VPCaNPs group (Fig. 8c). The secretion of proinflammatory cytokines, tumor necrosis factor alpha (TNF-α) and interferon gamma (IFN-γ), significantly raised in VPCaNPs group compared to other groups (Fig. 8d, e), indicating a strong proinflammatory effect. The polarization of tumor-associated macrophages (TAM) is also a hallmark of immune level[59,60]. As shown in Fig. 8f, the increased ratio of proinflammatory M_1-TAM ($CD11b^+F4/80^+CD86^+$) to anti-inflammatory M_2-TAM ($CD11b^+F4/80^+CD206^+$) indicated the destruction of immunosuppressive microenvironment. As the spleen is the primary site for the proliferation of myeloid-derived suppressor cells (MDSCs), another type of immune-suppressive cells, and a reservoir of $Ly6G^+$ MDSCs[61], we also measured the subpopulations of MDSCs (Fig. 8g and supplementary Fig. 14). Polymorphonuclear myeloid-derived suppressor cells (PMN-MDSCs, $CD11b^+Ly6C^-Ly6G^+$) showed significant decreases in VPCaNPs group compared to other groups. And the increase in non-MDSCs ($CD11b^+Ly6C^-Ly6G^-$) revealed reduced immunosuppression and decreased potential of MDSCs' recirculation. Ki67 is the proliferation symbol of cells and the immunofluorescence images (Fig. 8h) showed that CaNPs and VPCaNPs can significantly inhibit tumor cell proliferation. Furthermore, matrix metalloproteinase 9 (MMP9), an enzyme related to angiogenesis and metastasis[62,63], was reduced especially in CaNPs and VPCaNPs groups (Fig. 8i), explaining the fewer lung metastases in these groups to some extent.

Metabolism and biosafety of VPCaNPs

The safety of a drug is another key factor in clinical translation in addition to efficacy. After entering the body, nanoparticles may accumulate in other places in addition to target tissues, and they may produce toxic products during metabolism. To improve biosafety, we used biocompatible carriers (HA and PAA) with certain tumor selectivity. Upon contact with tumor cells, the HA within VPCaNPs can selectively bind with the overexpressed CD44 receptors on the cell surface, thereby prompting cellular uptake of the nanoparticles. The acidic tumor microenvironment makes PAA swell and release CaO_2 and VPQDs. Also, intracellular hyaluronidase can completely decompose HA, resulting in collapse of nanoparticles, and subsequent release of cargos. The reactions between CaO_2 and VPQDs have demonstrated above. And the non-degradable PAA can be taken up by the mononuclear phagocyte system and excreted through liver[64]. Additionally, VPCaNPs can be excreted through gastrointestinal tract within 5 days, which was confirmed by inductively coupled plasma mass spectrometry (ICP/MS) analysis of P (Supplementary Fig. 15).

Supplementary Fig. 16a illustrated that VPCaNPs administration induced a transient decrease in body weight followed by a continuous increase, indicating that VPCaNPs did not affect the quality of life for a

https://doi.org/10.1038/s41467-024-50769-0

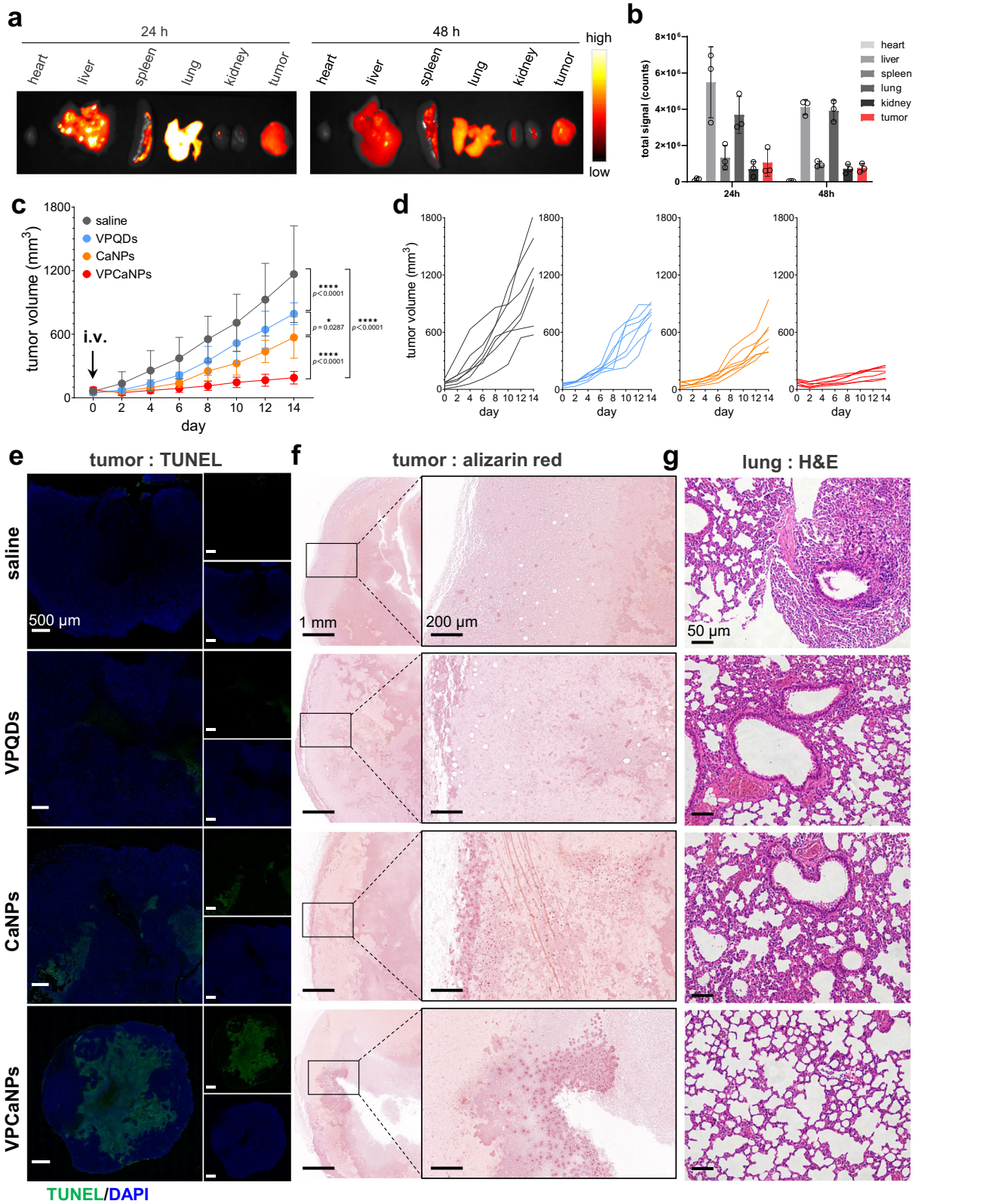

Fig. 7 | In vivo antitumor performance of nanosystems. a Fluorescence images of main organs and tumors 24 h and 48 h post *i.v.* administration of cy5-VPCaNPs and (**b**) corresponding fluorescence intensity. Data are presented as the mean with SD ($n = 3$ independent mice). **c**, **d** Antitumor performance of saline, VPQDs, CaNPs, and VPCaNPs post *i.v.* treatments on subcutaneous xenograft breast cancer animals. Data are presented as the mean with SD ($n = 7$ biologically independent mice). Statistical differences were analyzed by a two-way ANOVA with Tukey's multiple comparisons test. **e** TUNEL staining and (**f**) alizarin red staining tumors, and (**g**) H&E staining lungs of treated mice. The saline groups were control groups. Each experiment was repeated three times independently with similar results.

https://doi.org/10.1038/s41467-024-50769-0

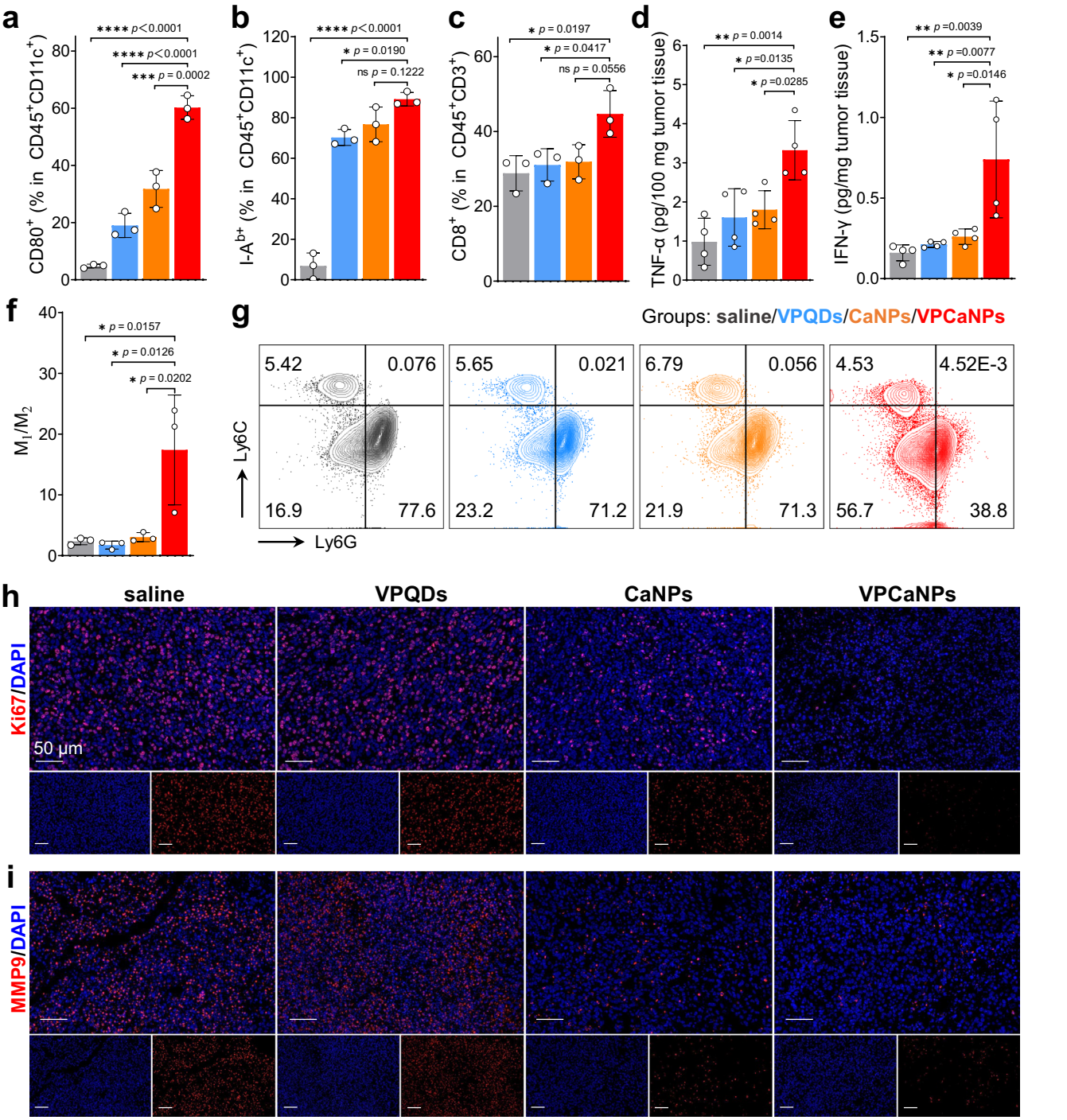

Fig. 8 | In vivo immune activated by VPCaNPs 14 days post *i.v.* administration. **a** Dendritic cells maturation ($CD45^+CD11c^+CD80^+$) and (**b**) activation ($CD45^+CD11c^+I\text{-}A^{b+}$) in draining lymph node. **c** Scale of tumor infiltrated cytotoxic T lymphocytes (CTL, $CD45^+CD3^+CD8^+$). **d** TNF-α and (**e**) IFN-γ contents in tumor tissues measured by ELISA. **f** Ratio of tumor infiltrated M_1 ($CD86^+$) to M_2 ($CD206^+$) tumor-associated macrophages (TAM, $CD45^+CD11b^+F4/80$). Data are presented as the mean with SD ($n = 3$) independent samples in (**a**–**c**, **f**), $n = 4$ independent samples in (**d**, **e**). Statistical differences were analyzed by a one-way ANOVA with Tukey's multiple comparisons test. **g** Scatter diagram of myeloid-derived suppressor cells (MDSCs, $CD11b^+Ly6C^+Ly6G^-$/$CD11b^+$ $Ly6C^-Ly6G^+$) in spleen. Immunofluorescence images of (**h**) Ki67 and (**i**) MMP9 of tumors. The saline groups were control groups. Each experiment was repeated three times independently with similar results.

long period of time. All groups exhibited normal results in blood routine and biochemical function tests (Supplementary Fig. 16b, c). Additionally, there was no significant difference in the concentrations of calcium ions and phosphate in the serum among saline, CaNPs, and VPCaNPs groups of mice while VPQDs group showing obvious higher P content compared with CaNPs and VPCaNPs groups (Supplementary Fig. 16d), suggesting that the nanoparticles did not remain in the systemic circulation but the ultrasmall VPQDs cannot be excreted in time. We also collected sections of major organs of mice 14 days after administration for H&E staining. As shown in Supplementary Fig. 17, the sections of heart, liver, spleen, and kidney from each group appeared normal though several organs showed an accumulation of nanoparticles (Fig. 7a, b). The results above indicate that intravenous administration of VPCaNPs exhibits significant anti-tumor efficacy

without causing notable systemic toxicity or side effects of functional damage, thus providing guarantees of both efficacy and safety for further drug research.

Discussion

Tumor nanocatalytic medicine relies on catalysts, substrates, and energy sources to produce or consume molecules that affect tumor survival. Catalytic generated-ROS can damage the structure and function of tumor cells and induce apoptosis[65]. In our study, the latest phosphorus allotrope, violet phosphorus, was prepared into quantum dots for catalyzing ROS generation, which was verified by both theoretical and experimental studies. For further application of VPQDs in vivo, CaO_2 served as the source of catalytic substrate O_2 and H_2O_2 (lacking in the tumor site) for preparing VPQDs and CaO_2-containing nanoparticles (VPCaNPs). VPCaNPs were capable of triggering ROS bursts in tumor cells, leading to cell death. In addition, CaO_2 in VPCaNPs can be rapidly decomposed into calcium ions under acidic conditions, with the generated oxygen further degrading VPQDs into phosphate, thereby facilitating tumor calcification. VPCaNPs can also activate body immune characterized as DCs activation, CTLs increase, TNF-α and IFN-γ secretion as well as the decrease of immunosuppressive cells (M_2-TAM and MDSCs) and proteins (Ki67 and MMP9). In summary, we presented a nanosystem that can provide both catalyst and substrate for a cytotoxic oxygen free radicals burst followed by tumor calcification induced by metabolites of the nanoparticle, leading to tumor inhibition and immune activation.

We mechanistically analyzed the ability of VP as a catalyst to generate ROS and observed its degradation in an oxygen-containing environment. However, from the perspective of the continuity of the reactions, the illustrated catalytic ability of VPQDs may only be the initial step in its degradation, i.e., the catalytic reaction described in this study may only occur in the initial stage of contact between VP and O_2 or H_2O_2. It has been reported that few-layer black phosphorus (BP) will degrade while generating ROS in the dark, oxygenated solutions[66]. Although VP has higher thermal stability than BP, the as-prepared VPQDs were ultrasmall and only 2–3 layers thick, leading to several reaction sites exposure to oxygen. In addition, we observed no ROS production in the aqueous solution, whereas ·OH production in the H_2O_2-containing solution. Therefore, with the generation of P vacancies, induced by contacting with O_2 or H_2O_2, the generated ROS may also be converted into each other. The specific mechanism should be different from the reported one and further research is needed.

Methods

Animals and ethical statement

All animal experiments in this study were carried out in compliance with all relevant ethical regulations and approved by the Experimental Animal Ethics Committee of the Institute of Radiological Medicine, Chinese Academy of Medical Sciences (Approval No. IRM-DWLL-2023070). Balb/c mice (female, 6–8-week-old) were purchased from SPF Biotechnology Co., Ltd. Beijing, China. All mice were raised in specific pathogen-free animal experimental center and allowed free access to food and water. All experimental/control animals were co-housed in a habitant under standard conditions (23–26 °C, 40–60% humidity, 12 h light–dark cycle, and 5 mice/cage). Animals with ulcerated tumors should receive immediate treatment with analgesics or be euthanized. According to the guidelines of ethics committee, the maximum tumor diameter should not exceed 20 mm in any dimension and the maximal tumor size permitted is 1500 mm^3. The maximal tumor size in this study was not exceeded. At the end point of the study, animal euthanasia was performed by CO_2 inhalation followed by cervical dislocation. Female mice were chosen because the primary population affected by breast cancer patients is female clinically[67].

Preparation of violet phosphorus quantum (VPQDs)

The VPQDs were synthesized through a sequence of modified liquid exfoliation and solvothermal reaction. In detail, the VP powder (Nanjing MKNANO Tech. Co., Ltd.) was ultrasound sonicated in deoxygenated N-Methyl-2-pyrrolidone (NMP) at the power of 600 W after fully triturated. The ultrasonic power is 600 W and the interval is 2 s on, 3 s off, and the whole process is carried out on the ice. A centrifugation process was carried out at 2775 × *g* for 10 min to get rid of bulk VP. The VP nanosheets/NMP suspension was then removed to Muffle furnace for solvothermal reaction for 16 h at 150 °C in a Teflon-lined reactor. The supernatant was collected by centrifugation at 43,000 × *g* for 30 min and concentrated through distillation at 120 °C in a decompression environment. NMP was removed by dialysis in ultra-pure water to obtain VPQDs for subsequent use.

Preparation of CaO_2 nanoparticles (CaNPs) and VP/CaO_2 nanoparticles (VPCaNPs)

Sodium hyaluronate (HA), polyacrylic acid (PAA), calcium chloride ($CaCl_2$) and synthesized VPQDs was added and dispersed in sequence into methanol. Afterwards, under ultrasonic bath, H_2O_2 was added dropwise into the mixture and then ammonia was added quickly. VPCaNPs was obtained by centrifugation and washed with ddH_2O. CaNPs can be prepared without adding VPQDs in the above process.

Electron spin resonance (ESR) of VPQDs

Generation of specific oxygen radicals was determined by ESR detector with different substrate supply. Two samples were prepared: oxygenated VPQDs aqueous solution and deoxygenated VPQDs solution with extra H_2O_2. VPQDs concentration is 20 μg/ml. Then 100 μl sample solution was mixed with 100 μl 5,5-Dimethyl-1-pyrroline N-oxide (DMPO, 100 mM, a popular spin trap) and sealed with a capillary tube to detect ·OH. As for detecting $\cdot O_2^-$, another 100 μl methanol was mixed with the sample and DMPO before sealing.

ROS generation in vitro

1,3-diphenylisobenzofuran (DPBF) is utilized as general a ROS probe. The DPBF stock solution was prepared by dissolving in DMSO at the concentration of 1 mg/ml. The total reaction volume was 1.5 ml containing 100 μl DPBF stock. The oxygenated condition was prepared by bubbling pure oxygen for 20 s and the H_2O_2 concentration was 100 μM in H_2O_2-sufficient solution. The testing concentration of VPQDs was at 20 μg/ml.

Calculation details

The first-principles calculations based on DFT were carried out using Vienna ab initio simulation package (VASP, version 5.4) code[68–70]. Perdew-Burke-Ernzerhof (PBE) generalized gradient approximation (GGA) was adopted to treat the electron exchange-correlation functional[71]. Grimme's DFT-D2 method was taken into consideration to describe the van der Waals (VDW) forces[72]. The energy cut-off for expansion of plane-wave expansion was set to be 500 eV. The Brillouin zone was sampled by 2 × 2 × 1 Monkhorst-Pack *k*-point meshes. The convergence threshold was set to be 1×10^{-5} Ha for total energy and 0.01 Ha/Å for atomic forces, respectively. To prevent interlayer interference, a vacuum space of 20 Å in *c*-direction was added to both pristine and adsorbed VP models. The initial adsorption sites for catalytic pathway were search by Monte Carlo (MC) annealing simulations, which allow a rotatable molecule to randomly translate on the surface of the substrate until the local energy minima reached[73–76]. Although no simple a posteriori correction scheme is implemented in VASP for slab calculations presently, the charged calculations were just applied for qualitative prediction of the trends and mechanism of catalytic reactions[77]. Considering that the charged computations involved in this work are both single-component systems (positively charged VP and $\cdot O_2^-$). Here, charged calculations were accomplished

by adjusting the NELECT parameter, which governs the total valence electron count of the whole system.

Cytotoxicity test

Human embryonic kidney cells (HEK-293T, cat#GNHu17), mouse fibroblasts cells (L929, cat#SCSP-5039), and mouse breast cancer cells (4T1, cat#TCM32) obtained from the National Collection of Authenticated Cell Cultures (NCACC) were selected for cytotoxicity test. No cell line was contaminated with mycoplasma. HEK-293T and L929 cells were cultured in basal DMEM medium (Gibco) supplemented with 10% FBS (Pricella), 1% Penicillin–Streptomycin Solution (Gibco) at 37 °C in 5% CO_2. The basal medium of the 4T1 cell line is RPMI 1640 (Gibco). Logarithmic cells were collected and inoculated on 96-well cell culture plate at a density of 5000 cells/well. After incubating for 24 h, culture medium containing different concentrations of VPQDs (0, 2.5, 5, 10, 20 μg/ml, measured by P), CaNPs and VPCaNPs (0, 5, 10, 20, 40 μg/ml, measured by Ca) was replaced. The cell activity was measured by CCK8 method with 4 parallel holes for each concentration.

Flow cytometry analysis

Logarithmic 4T1 cells were collected and inoculated into 6-well plates at a density of 10^5/well for 24 h. After loading with ROS probe (DCFH-DA), O_2 probe ($[Ru(dpp)_3]Cl_2$), and specific probes of ·OH, H_2O_2, $·O_2^-$, Ca^{2+} and probes, respectively, medium containing VPQDs, CaNPs, and VPCaNPs was replaced and incubated for 6 h. To measure lipid peroxidation level, C11-BODIPY$^{581/591}$-loaded cells were incubated with nanomaterials for 12 h before collecting cells. JC-1 and apoptosis markers (PI and Annexin V-FITC) were utilized after nanomaterials incubation for 12 h. All cells were collected after administration and dyeing for flow cytometry. Signals in FITC channel were recorded for ROS, ·OH, H_2O_2, Ca^{2+} and $·O_2^-$, and signal in PE channel was collected for O_2. Both FITC and PI signals were collected for JC-1, lipid peroxidation, and apoptosis. All flow cytometry data was analyzed by FlowJo.

To evaluate the antitumor immune function, single-cell suspensions were prepared 14 d post-administration. Tissues of the tumor, spleen, and tumor-draining lymph node were dissociated and ground through a cellular sieve. Collagenase and DNase incubation was necessary before tumor tissue grinding. If desired, the red blood cells can be lysed before dying. After incubation with an anti-mouse CD16/CD32 antibody (Invitrogen, cat#14-0161-82, 93, dilution: 1:200) for 10 min to block Fcγ receptors, surface staining was performed with different combinations of antibodies against the following mouse proteins: CD45 (Biolegend, cat#103115, 30-F11, dilution: 1:250), CD11c (Biolegend, cat#117306, N418, dilution: 1:400), CD80 (Biolegend, cat#104721, 16-10A1, dilution: 1:100), CD3 (Biolegend, cat#100204, 17A2, dilution: 1:200), CD8a (Biolegend, cat#100707, 53-6.7, dilution: 1:1000), CD11b (Biolegend, cat#101206, M1/70, dilution: 1:600), F4/80 (Biolegend, cat#123131, BM8, dilution: 1:200), CD206 (Biolegend, cat#141708, C068C2, dilution: 1:500), Ly6C (Biolegend, cat#128008, HK1.4, dilution: 1:200), Ly6G (Biolegend, cat#127614, 1A8, dilution: 1:500). The gating strategies were shown in Supplementary Figs. 18–21.

Cell calcification

4T1 cells were stained with DiD for general cell membrane labeling and then plated onto glass bottom cell dishes. After cell adherent, cultures containing saline, VPQDs, CaNPs, and VPCaNPs were added to the cell dishes. After incubating for another 48 h, the cells were fixed with 4% paraformaldehyde for 15 min at room temperature and then stained with DAPI for 10 min. Afterward, the cells were washed with PBS, and calcein (Ex. 495 nm, Em. 515 nm) was added for another 20 min before the cells were washed with PBS again and subjected to CLSM.

To collect the cell secretions, cells were cultivated with saline, VPQDs, CaNPs and VPCaNPs at 37 °C for 48 h. Afterwards, the cells and medium were harvested and centrifuged at 2775 × *g* for 10 min, and the product was washed twice with a chloroform/cyclohexane/ethanol mixture. The centrifuged deposit was then dried at 60 °C in an oven, and a white powder was obtained for XRD analysis.

Cell migration

First, 5×10^4 4T1 cells were plated into transwell plates (Corning) with RPMI 1640 medium containing saline, VPQDs, CaNPs, and VPCaNPs. After 24 h, the cells were fixed with paraformaldehyde for 15 min. Cells in the upper chambers were wiped away, and cells on the submembrane surface were counted through optical microscope. In total, 5 random views were chosen for each hole to represent the total number of cells in each well. This experiment was repeated 3 times.

In vivo anti-tumor study

The 6–8-week-old female BALB/c mice were selected for subcutaneous modeling in situ. The tumor-bearing mice were randomly divided into saline, VPQDs, CaNPs, and VPQDs + CaNPs groups for intratumoral administration and saline, VPQDs, CaNPs, and VPCaNPs groups for intravenous administration. The tumor size and body weight were measured every other day for total 14 days. The tumor volume was calculated according to the formula $V = L \times W^2/2$, where L and W denoted the maximum tumor length and width. Statistical analysis was performed in every group, and the error bar represents the standard deviation of the relative tumor volume. On the 14 day post systematic administration, blood of mice was collected for routine and biochemical tests. All the tumor tissues were dissected for alizarin red staining and TUNEL immunofluorescent analysis, and the major organs were also dissected for histological analysis.

Sample preparation of ICP/MS

On day 1, 3, 5, 7, 10 post i.v. administration with VPCaNPs, urine and feces of mice were collected. The urine samples were centrifuged at 650 × *g* for 6 min and the supernatant was for detection. 50 mg of feces were added into 450 μl saline for homogenate. Then centrifuge at 1000 × *g* for 10 min and take the supernatant for detection.

Statistical analysis

Graph Pad Prism 8.0 and Origin 9.0 were used for data statistics and statistical significance calculation. Statistical analysis was performed using the Student's *t* test and one/two-way ANOVA. The specific method is indicated in the captions of figures. Asterisks (*) were used as significant differences. *P* values less than 0.0001 were shown as <0.0001 and summarized with four asterisks (****). *P* values less than 0.001, 0.01, 0.05 are summarized with three (***), two (**), and one (*) asterisk(s), respectively.

Reporting summary

Further information on research design is available in the Nature Portfolio Reporting Summary linked to this article.

Data availability

The authors declare that all data supporting the findings of this study are available within the article and the Supplementary Information. The full image dataset is available from the corresponding author upon request. Source data are provided with this paper.

References

1. Yang, B., Chen, Y. & Shi, J. Nanocatalytic medicine. *Adv. Mater.* **31**, e1901778 (2019).
2. Lu, X., Gao, S., Lin, H. & Shi, J. Single-atom catalysts for nanocatalytic tumor therapy. *Small* **17**, e2004467 (2021).
3. Wu, C. et al. A nonferrous ferroptosis-like strategy for antioxidant inhibition-synergized nanocatalytic tumor therapeutics. *Sci. Adv.* **7**, eabj8833 (2021).

4. Sun, Z. et al. Self-propelled Janus nanocatalytic robots guided by magnetic resonance imaging for enhanced tumor penetration and therapy. *J. Am. Chem. Soc.* **145**, 11019–11032 (2023).
5. Raj, L. et al. Selective killing of cancer cells by a small molecule targeting the stress response to ROS. *Nature* **475**, 231–234 (2011).
6. Xu, K. et al. Multienzyme-mimicking $LaCoO_3$ nanotrigger for programming cancer-cell pyroptosis. *Adv. Mater.* **35**, e2302961 (2023).
7. Fan, Y. et al. Biomimetic piezoelectric nanomaterial-modified oral microrobots for targeted catalytic and immunotherapy of colorectal cancer. *Sci. Adv.* **10**, eadm9561 (2024).
8. Ouyang, J. et al. Minimally invasive nanomedicine: nanotechnology in photo-/ultrasound-/radiation-/magnetism-mediated therapy and imaging. *Chem. Soc. Rev.* **51**, 4996–5041 (2022).
9. Bonnet, S. Ruthenium-based photoactivated chemotherapy. *J. Am. Chem. Soc.* **145**, 23397–23415 (2023).
10. Gu, T. et al. Platinum nanoparticles to enable electrodynamic therapy for effective cancer treatment. *Adv. Mater.* **31**, e1806803 (2019).
11. Cheng, Y., Xia, Y. D., Sun, Y. Q., Wang, Y. & Yin, X. B. "Three-in-one" nanozyme composite for augmented cascade catalytic tumor therapy. *Adv. Mater.* **36**, 2308033 (2023).
12. Wang, L. C. et al. Atomically dispersed golds on degradable zerovalent copper nanocubes augment oxygen driven Fenton-like reaction for effective orthotopic tumor therapy. *Nat. Commun.* **13**, 7772 (2022).
13. Huo, M., Wang, L., Chen, Y. & Shi, J. Tumor-selective catalytic nanomedicine by nanocatalyst delivery. *Nat. Commun.* **8**, 357 (2017).
14. Martinez-Reyes, I. & Chandel, N. S. Cancer metabolism: looking forward. *Nat. Rev. Cancer* **21**, 669–680 (2021).
15. Lee, P., Chandel, N. S. & Simon, M. C. Cellular adaptation to hypoxia through hypoxia inducible factors and beyond. *Nat. Rev. Mol. Cell Biol.* **21**, 268–283 (2020).
16. Chu, Z. et al. Recent advances on modulation of H_2O_2 in tumor microenvironment for enhanced cancer therapeutic efficacy. *Coord. Chem. Rev.* **481**, 215049 (2023).
17. Fenton, H. J. H. LXXIII.—Oxidation of tartaric acid in presence of iron. *J. Chem. Soc. Trans.* **65**, 899–910 (1894).
18. Hassannia, B., Vandenabeele, P. & Vanden Berghe, T. Targeting ferroptosis to iron out cancer. *Cancer Cell* **35**, 830–849 (2019).
19. Zhao, P., Li, H. & Bu, W. A forward vision for chemodynamic therapy: issues and opportunities. *Angew. Chem. Int. Ed.* **62**, e202210415 (2023).
20. Shi, J., Kantoff, P. W., Wooster, R. & Farokhzad, O. C. Cancer nanomedicine: progress, challenges and opportunities. *Nat. Rev. Cancer* **17**, 20–37 (2017).
21. Shao, X. et al. Intrinsic bioactivity of black phosphorus nanomaterials on mitotic centrosome destabilization through suppression of PLK1 kinase. *Nat. Nanotechnol.* **16**, 1150–1160 (2021).
22. Zhang, L. et al. Structure and properties of violet phosphorus and its phosphorene exfoliation. *Angew. Chem. Int. Ed.* **59**, 1074–1080 (2019).
23. Zhao, R. et al. Violet phosphorus quantum dots. *J. Mater. Chem. A* **10**, 245–250 (2022).
24. Zhao, R. et al. Wide bandgap tuning of violet phosphorus quantum dots by functionalization. *J. Phys. Chem. Lett.* **13**, 8236–8244 (2022).
25. Holder, C. F. & Schaak, R. E. Tutorial on powder X-ray diffraction for characterizing nanoscale materials. *ACS Nano* **13**, 7359–7365 (2019).
26. Holzwarth, U. & Gibson, N. The Scherrer equation versus the 'Debye-Scherrer equation. *Nat. Nanotechnol.* **6**, 534 (2011).
27. Zhang, L. et al. Fast identification of the crystallographic orientation of violet phosphorus nanoflakes with preferred in-plane cleavage edge orientation. *Adv. Funct. Mater.* **32**, 2111057 (2022).
28. Lu, Y. L. et al. Fibrous red phosphorene: a promising two-dimensional optoelectronic and photocatalytic material with a desirable band gap and high carrier mobility. *Phys. Chem. Chem. Phys.* **22**, 13713–13720 (2020).
29. He, W., Cai, J., Jiang, X., Yin, J. J. & Meng, Q. Generation of reactive oxygen species and charge carriers in plasmonic photocatalytic $Au@TiO_2$ nanostructures with enhanced activity. *Phys. Chem. Chem. Phys.* **20**, 16117–16125 (2018).
30. Liu, H. et al. Polarization-sensitive photodetectors based on highly in-plane anisotropic violet phosphorus with large dichroic ratio. *Adv. Funct. Mater.* **34**, 2314838 (2023).
31. Lu, Y. L. et al. Hittorf's violet phosphorene as a promising candidate for optoelectronic and photocatalytic applications: first-principles characterization. *Phys. Chem. Chem. Phys.* **20**, 11967–11975 (2018).
32. Siahrostami, S., Li, G. L., Viswanathan, V. & Norskov, J. K. One- or two-electron water oxidation, hydroxyl radical, or H_2O_2 evolution. *J. Phys. Chem. Lett.* **8**, 1157–1160 (2017).
33. Qin, X. et al. Peroxisome inspired hybrid enzyme nanogels for chemodynamic and photodynamic therapy. *Nat. Commun.* **12**, 5243 (2021).
34. Zeng, G. et al. Hydroxyl radicals in natural waters: light/dark mechanisms, changes and scavenging effects. *Sci. Total Environ.* **868**, 161533 (2023).
35. Zhang, X. et al. A stable low-temperature H_2-production catalyst by crowding Pt on alpha-MoC. *Nature* **589**, 396–401 (2021).
36. Zhu, Y. et al. Stimuli-responsive manganese single-atom nanozyme for tumor therapy via integrated cascade reactions. *Angew. Chem. Int. Ed.* **60**, 9480–9488 (2021).
37. Chen, Z. X. et al. Interfering with lactate-fueled respiration for enhanced photodynamic tumor therapy by a porphyrinic MOF nanoplatform. *Adv. Funct. Mater.* **28**, 1803498 (2018).
38. Wu, D. et al. Efficacy-shaping nanomedicine by loading calcium peroxide into tumor microenvironment-responsive nanoparticles for the antitumor therapy of prostate cancer. *Theranostics* **10**, 9808–9829 (2020).
39. Zhang, S. et al. A novel strategy for tumor therapy: targeted, PAA-functionalized nano-hydroxyapatite nanomedicine. *J. Mater. Chem. B* **8**, 9589–9600 (2020).
40. Li, F. et al. Investigation of glyphosate removal from aqueous solutions using Fenton-like system based on calcium peroxide. *Processes* **10**, 2045 (2022).
41. Zhang, M. et al. Calcium-overload-mediated tumor therapy by calcium peroxide nanoparticles. *Chem* **5**, 2171–2182 (2019).
42. Xiong, J. et al. CN/rGO@BPQDs high-low junctions with stretching spatial charge separation ability for photocatalytic degradation and H_2O_2 production. *Appl. Catal. B-Environ. Energy* **266**, 118602 (2020).
43. Lian, Q. et al. The effects of carbon disulfide driven functionalization on graphene oxide for enhanced Pb(II) adsorption: Investigation of adsorption mechanism. *Chemosphere* **248**, 126078 (2020).
44. Alemdar, S., Basak, A. & Metin, O. Exploring the enhanced catalytic activity of Pt nanoparticles generated on the red phosphorus/graphitic carbon nitride binary heterojunctions in the photo-assisted hydrolysis of ammonia borane. *ACS Appl. Mater. Interfaces* **15**, 48096–48109 (2023).
45. Eroglu, Z., Ozer, M. S. & Metin, O. Black phosphorus quantum dots/carbon nitride-reduced graphene oxide ternary heterojunction as a multifunctional metal-free photocatalyst for photooxidation reactions. *ACS Sustain. Chem. Eng.* **11**, 7560–7572 (2023).
46. Ren, X., Yang, X., Xie, G. & Luo, J. Black phosphorus quantum dots in aqueous ethylene glycol for macroscale superlubricity. *ACS Appl. Nano Mater.* **3**, 4799–4809 (2020).
47. Zhang, H. et al. Redox regulation and its emerging roles in cancer treatment. *Coord. Chem. Rev.* **475**, 214897 (2023).

48. Nappi, A. J. & Vass, E. Hydroxyl radical production by ascorbate and hydrogen peroxide. *Neurotox. Res.* **2**, 343–355 (2000).
49. Pinton, P., Giorgi, C., Siviero, R., Zecchini, E. & Rizzuto, R. Calcium and apoptosis: ER-mitochondria Ca^{2+} transfer in the control of apoptosis. *Oncogene* **27**, 6407–6418 (2008).
50. Brouwers, J. F., Silva, P. F. & Gadella, B. M. New assays for detection and localization of endogenous lipid peroxidation products in living boar sperm after BTS dilution or after freeze-thawing. *Theriogenology* **63**, 458–469 (2005).
51. Wu, J. et al. Bioinspired tumor calcification enables early detection and elimination of lung cancer. *Adv. Funct. Mater.* **31**, 2101284 (2021).
52. Tang, N. et al. A macromolecular drug for cancer therapy via extracellular calcification. *Angew. Chem. Int. Ed.* **60**, 6509–6517 (2021).
53. Shou, H., Wu, J., Tang, N. & Wang, B. Calcification-based cancer diagnosis and therapy. *ChemMedChem* **17**, e202100339 (2022).
54. Yuan, X. et al. Self-triggered thermoelectric nanoheterojunction for cancer catalytic and immunotherapy. *Nat. Commun.* **14**, 5140 (2023).
55. Kitamura, T., Qian, B.-Z. & Pollard, J. W. Immune cell promotion of metastasis. *Nat. Rev. Immunol.* **15**, 73–86 (2015).
56. Krysko, D. V. et al. Immunogenic cell death and DAMPs in cancer therapy. *Nat. Rev. Cancer* **12**, 860–875 (2012).
57. Kang, Y. et al. Calcium-based nanotechnology for cancer therapy. *Coord. Chem. Rev.* **481**, 215050 (2023).
58. Philip, M. & Schietinger, A. $CD8^+$ T cell differentiation and dysfunction in cancer. *Nat. Rev. Immunol.* **22**, 209–223 (2021).
59. Zhang, D. et al. Metabolic regulation of gene expression by histone lactylation. *Nature* **574**, 575–580 (2019).
60. Mantovani, A., Sozzani, S., Locati, M., Allavena, P. & Sica, A. Macrophage polarization: tumor-associated macrophages as a paradigm for polarized M_2 mononuclear phagocytes. *Trends Immunol.* **23**, 549–555 (2002).
61. Talmadge, J. E. & Gabrilovich, D. I. History of myeloid-derived suppressor cells. *Nat. Rev. Cancer* **13**, 739–752 (2013).
62. Biswas, S. K. Metabolic reprogramming of immune cells in cancer progression. *Immunity* **43**, 435–449 (2015).
63. De Palma, M., Biziato, D. & Petrova, T. V. Microenvironmental regulation of tumour angiogenesis. *Nat. Rev. Cancer* **17**, 457–474 (2017).
64. Ruman, U., Fakurazi, S., Masarudin, M. J. & Hussein, M. Z. Nanocarrier-based therapeutics and theranostics drug delivery systems for next generation of liver cancer nanodrug modalities. *Int. J. Nanomed.* **15**, 1437–1456 (2020).
65. Sies, H., Berndt, C. & Jones, D. P. Oxidative stress. *Annu. Rev. Biochem.* **86**, 715–748 (2017).
66. Yu, W. et al. Unexpected persistent production of reactive oxygen species during the degradation of black phosphorous in the darkness. *Angew. Chem. Int. Ed.* **61**, e202213595 (2022).
67. Zhou, M. et al. Cell surface patching via CXCR4-targeted nanothreads for cancer metastasis inhibition. *Nat. Commun.* **15**, 2763 (2024).
68. Kresse, G. & Hafner, J. Ab initio molecular dynamics for liquid metals. *Phys. Rev. B* **47**, 558–561 (1993).
69. Kresse, G. & Hafner, J. Ab initio molecular-dynamics simulation of the liquid-metal-amorphous-semiconductor transition in germanium. *Phys. Rev. B* **49**, 14251–14269 (1994).
70. Kresse, G. & Furthmüller, J. Efficiency of ab-initio total energy calculations for metals and semiconductors using a plane-wave basis set. *Comp. Mater. Sci.* **6**, 15–50 (1996).
71. Perdew, J. P., Burke, K. & Ernzerhof, M. Generalized gradient approximation made simple. *Phys. Rev. Lett.* **77**, 3865–3868 (1996).
72. Grimme, S. Semiempirical GGA-type density functional constructed with a long-range dispersion correction. *J. Comput. Chem.* **27**, 1787–1799 (2006).
73. Khaled, K. F. Electrochemical behavior of nickel in nitric acid and its corrosion inhibition using some thiosemicarbazone derivatives. *Electrochim. Acta* **55**, 5375–5383 (2010).
74. Musa, A. Y., Jalgham, R. T. T. & Mohamad, A. B. Molecular dynamic and quantum chemical calculations for phthalazine derivatives as corrosion inhibitors of mild steel in 1M HCl. *Corros. Sci.* **56**, 176–183 (2012).
75. Kang, Y. et al. Design of a two-dimensional interplanar heterojunction for catalytic cancer therapy. *Nat. Commun.* **13**, 2425 (2022).
76. Chen, L. et al. Edge modification facilitated heterogenization and exfoliation of two-dimensional nanomaterials for cancer catalytic therapy. *Sci. Adv.* **8**, eabo7372 (2022).
77. Liu, J. et al. DFT computation of Cu adsorption on the S atoms of sphalerite (110) surface. *Miner. Eng.* **46-47**, 1–5 (2013).

Acknowledgements

This study was supported by the National Natural Science Foundation of China (Grant No. 32301131, Z.M. and Grant No. 82272154, L.M.), Tianjin Science Fund for Distinguished Young Scholars (Grant No. 22JCJQJC00120, L.M.), the National Key Research and Development Program of China (Grant No. 2022YFE0139800, L.M.), the Fundamental Research Funds for the Central Universities (Grant No. 2021-RC310-005, L.M. and Grant No. 3332022070, Z.M.), Science and Technology Program of Tianjin City (the Basic Research Cooperation Special Foundation of Beijing-Tianjin-Hebei Region, Grant No. 22JCZXJC00060, L.M.), Chinese Academy of Medical Sciences Innovation Fund for Medical Sciences (Grant No. 2021-I2M-1-058, 2022-I2M-2-003, L.M. and Grant No. 2022-I2M-1-023, Z.M.), and the Fellowship of China Postdoctoral Science Foundation (Grant No. 2021M700502, Z.M.). Thank Professor Ping Wu from School of Science, Tianjin University for calculation resources. Especially thank Professor Jinying Zhang from Xi'an Jiaotong University for her guidance on synthesizing and verifying VPQDs.

Author contributions

H. Zhang, Z. Mao, and L. Mei designed and supervised the project. H. Zhang, Z. Mao, YS. Zhang, and L. Mei designed the experimental strategies. H. Zhang, Z. Mao, YT. Zhang, and H. Li, performed the experiments. H. Zhang, Z. Mao, Y. Yu, F. Zhang, W. Li, H. Yin and M. Ou analyzed the data. H. Zhang, Z. Mao, and L. Mei wrote the manuscript.

Competing interests

The authors declare no competing interests.

Additional information

Supplementary information The online version contains supplementary material available at https://doi.org/10.1038/s41467-024-50769-0.

Correspondence and requests for materials should be addressed to Zhuo Mao or Lin Mei.

Peer review information *Nature Communications* thanks the anonymous reviewers for their contribution to the peer review of this work. A peer review file is available.